Dyes and Pigments 232 (2025) 112455

Contents lists available at ScienceDirect

Dyes and Pigments

journal homepage: www.elsevier.com/locate/dyepig

Synthesis, characterization and application of quinoxaline-based organic dyes as anodic sensitizers in photoelectrochemical cells

Xheila Yzeiri [a,b,1], Nicola Sangiorgi [c,1], Francesca Gambassi [d], Andrea Barbieri [d], Massimo Calamante [b,e], Daniele Franchi [b], Carmen Coppola [a,b,f], Adalgisa Sinicropi [a,b,f], Barbara Ventura [d], Alessandro Mordini [b,e], Alessandra Sanson [c], Lorenzo Zani [b,*]

[a] Department of Biotechnology, Chemistry and Pharmacy, University of Siena, Via A. Moro 2, 53100, Siena, Italy
[b] Institute of Chemistry of Organometallic Compounds (CNR-ICCOM), Via Madonna del Piano 10, 50019, Sesto Fiorentino, Italy
[c] Institute of Science, Technology and Sustainability for Ceramics (CNR-ISSMC), Via Granarolo 64, 48018, Faenza, Italy
[d] Institute for Organic Synthesis and Photoreactivity (CNR-ISOF), Via P. Gobetti 101, 40129, Bologna, Italy
[e] Department of Chemistry "U. Schiff", University of Florence, Via della Lastruccia 13, 50019, Sesto Fiorentino, Italy
[f] Consorzio per lo Sviluppo dei Sistemi a Grande Interfase (CSGI), Via della Lastruccia 3, 50019, Sesto Fiorentino, Italy

ARTICLE INFO

Keywords:
Organic dyes
Photoelectrochemical cells
Photoanodes
Hydrogen
Artificial photosynthesis

ABSTRACT

Three new D-A-π-A organic dyes (**1a-c**) containing a 2,3-diphenylquinoxaline core as the main chromophore were designed to act as sensitizers for the TiO_2-based photoanode of dye-sensitized photoelectrochemical cells (DS-PEC) for water splitting. The dyes structures featured a cyanoacrylic acid group as the terminal acceptor/anchoring moiety and three different donor groups of moderate strength, namely mono- and dialkoxy-substituted benzenes, which were introduced to modulate the energies of the respective HOMO levels and enable the electron transfer from a Ru-based molecular water oxidation catalyst (WOC). Dyes **1a-c** were synthesized following a C–H activation strategy and fully characterized. In addition, the previously known catalyst **Ru(bda)(PyP)$_2$** (bda = 2,2′-bipyridine-6,6′-dicarboxylate; PyP = pyridin-4-methyl phosphonic acid) was also prepared by modification of a reported procedure. The dynamics of charge transfer processes involving the dyes adsorbed on nanocrystalline TiO_2 films were investigated by means of transient absorption spectroscopy. Photoelectrochemical experiments carried out on photoanodes functionalized with **1a-c** and **Ru(bda)(PyP)$_2$** in 0.1 M aq. Na_2SO_4 electrolyte showed the production of photocurrents up to ca. 0.15 mA cm^{-2} at + 0.5 V *vs.* NHE, and highlighted how modifications of the TiO_2 staining procedure can lead to significant differences in cell performances.

1. Introduction

In recent years, the potential use of hydrogen as a sustainable energy vector in place of fossil fuels has received increasing attention both from the scientific community and the industrial sector, due to its remarkable features of high specific energy, low carbon footprint and the possibility of being directly converted to electricity in fuel cells [1]. Nevertheless, molecular hydrogen (H_2) for industrial use is still mostly produced from methane through the steam-reforming reaction, causing significant greenhouse gases emissions [2]. To enable its use as an energy carrier, it is therefore mandatory to develop a more environmentally friendly process for H_2 generation on large scale. In this context, water electrolysis powered by renewable energy sources currently appears the most mature and readily applicable technology [3–5], but several other approaches are being investigated, including the direct conversion of water to oxygen and hydrogen by means of photocatalytic (PC) [6–8] or photoelectrochemical (PEC) [9,10] processes driven by solar light.

Concerning the latter, a number of different device architectures have been described in the literature, among which Dye-Sensitized Photoelectrochemical cells (DS-PECs) have been the subject of many studies in the last decade [11–14]. DS-PEC are constituted by a (photo) anode and a (photo)cathode, where water oxidation and reduction take place, respectively, connected by a metallic wire and immersed in an aqueous electrolyte solution. In the most common configuration (Fig. 1),

* Corresponding author.
E-mail address: lorenzo.zani@iccom.cnr.it (L. Zani).
[1] These authors contributed equally.

https://doi.org/10.1016/j.dyepig.2024.112455
Received 26 July 2024; Received in revised form 10 September 2024; Accepted 12 September 2024
Available online 14 September 2024

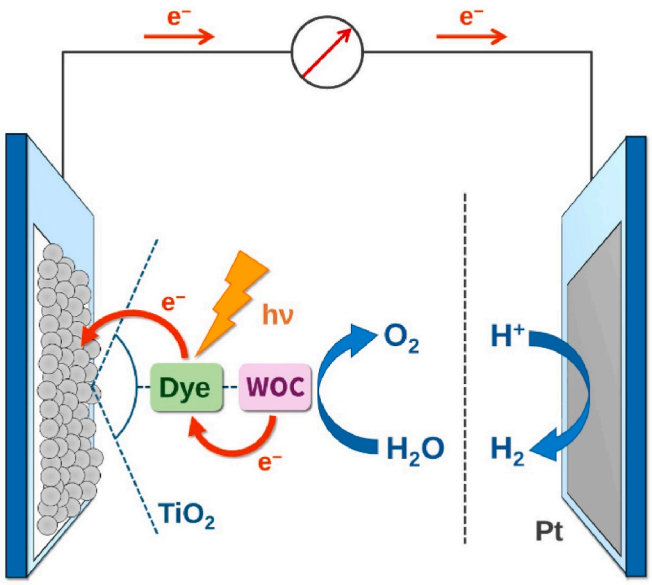

Fig. 1. General structure and working mechanism of a DS-PEC with an active photoanode.

the photoactive electrode is the photoanode, which is usually made by a thin film of a wide band gap semiconductor (such as TiO_2) deposed on a layer of a transparent conductive oxide (TCO) and sensitized towards visible light absorption by a molecular dye, while the cathode is constituted by an efficient catalytic material for hydrogen evolution reaction (typically platinum wire or mesh). Therefore, the fundamental structure of a DS-PEC is closely related to that of the well-developed Dye-Sensitized Solar Cell (DSSC) for electricity production [15], albeit with some significant differences. In particular, since water oxidation is a thermodynamically and kinetically challenging process, requiring transfer of 4 holes to form one molecule of oxygen, the photoanode is also usually functionalized with an appropriate water oxidation catalyst (WOC) [16,17], able to promote such reaction.

The working mechanism of a DS-PEC having the structure shown in Fig. 1 can be briefly summarized as follows [18]. Upon absorption of visible light, the sensitizer undergoes a photoexcitation process, promoting an electron from its highest occupied molecular orbital (HOMO) to the lowest unoccupied molecular orbital (LUMO). The excited electron is then injected into the conduction band (CB) of the semiconductor, and the resulting hole on the sensitizer is transferred to the WOC. The injected electrons then diffuse through the semiconductor to the TCO layer, and from there travel along the external circuit to reach the platinum cathode, where they are used for hydrogen generation via proton reduction. Meanwhile, the holes accumulated on the WOC by multiple transfers from oxidized dye molecules are employed to drive the oxygen evolution reaction, completing the process. Accordingly, to ensure a proper functioning of the cell, the WOC must be able, on the one hand, to regenerate the oxidized dye molecules after charge injection, and on the other to store the appropriate amount of oxidizing equivalents (holes) for the water oxidation to occur [19]. For this reason, it is typically constituted by a complex of a transition metal able to attain several consecutive oxidation states, such as ruthenium [20,21].

From the above discussion, it clearly emerges that dye-sensitization plays a central role in the cell working mechanism, since it is involved in some of its most crucial steps, namely light harvesting and charge separation. As a consequence, the dye used in a DS-PEC must present some peculiar features, including: (i) wide and intense light absorption in the visible region, (ii) robust anchoring to the semiconductor, (iii) appropriate frontier energy levels alignment to ensure electron transfer in the correct direction, (iv) sufficient chemical and photochemical stability.

Similar to DSSCs, initial reports concerning DS-PECs described the use of Ru-bipyridyl complexes and related species as dye sensitizers[11, 22–27], owing to their good optical and electrochemical properties. However, while in the case of DSSCs the attention of the researchers progressively shifted to the use of organic dyes, which have been the subject of countless studies [15] and currently hold some of the best performances in terms of power conversion efficiency [28–30], the use of metal-free dyes in DS-PECs has remained less developed [31], and studies have rather focused on optimizing other aspects of the cells, such as the composition and deposition of the anodic semiconductors [32–36] or the construction of complex supramolecular architectures to enhance charge separation and suppress charge recombination events [37–40]. Consequently, many of the reports dealing with the use of organic dyes for DS-PEC describe the application of small and relatively simple donor-acceptor molecules [41–43], often featuring plain thiophene rings as conjugated spacers [34,44,45], and therefore showing weak light-harvesting ability in the middle of the visible region, where the emission spectrum of sunlight is maximized (>500 nm) [46,47]. Notable exceptions, albeit limited in number, include the use of sensitizers containing phenothiazine [48], quinacridone [49], perylene [50], subporphyrin [51] and porphyrin (not strictly metal-free) [52] units, sometimes also combined with the WOC through different strategies to form dye-catalyst molecular dyads [53–56].

Despite that, replacing Ru-based dyes with fully organic sensitizers in photoelectrochemical cells could be potentially advantageous thanks to their properties of lower cost, absence of critical or precious metals, simple synthesis and tunable spectroscopic properties. For this reason, building on our previous experience on the synthesis and application of organic dyes in three-component photocatalytic systems for hydrogen production [57–61], we turned our attention to the development of novel donor-π-acceptor (D-π-A) organic sensitizers showing both improved light-harvesting capability and optimized electrochemical properties for employment in DS-PEC. To fulfill this objective, we designed the structures of the new compounds according to the following basic principles: (i) in their conjugated structure, the dyes should feature an heterocyclic chromophore able to impart strong absorption in the visible region, possibly with maximum close to 500 nm and an onset around 600 nm; (ii) the sensitizers should present donor groups of moderate strength, so as to modulate their ground-state oxidation potentials (E_{ox}) and make them compatible with the most common WOCs (*e. g.* Ru-bda complexes) [20]; (iii) alkyl chains present on the compounds structures could make them more soluble in common organic solvents, facilitating their purification and subsequent handling; (iv) the compounds structures should be easily obtained through a modular synthetic sequence allowing late-stage differentiation.

Based on the above considerations, we designed compounds **1a-c**, featuring a 2,3-diphenylquinoxaline core as their main chromophore (Fig. 2). Such central unit was selected because it had been already successfully incorporated in several organic sensitizers for dye-sensitized solar cells [62] and we also observed that D-A organic compounds containing a quinoxaline moiety as the central acceptor exhibited intense light absorption in the visible region [63,64].

In compounds **1a-c**, the quinoxaline unit was flanked by two thiophene rings, introduced to further extend the conjugation length of the structures and thus red-shift their absorption spectra, and a typical cyanoacrylic acid moiety was chosen as the anchoring function in all cases. On the contrary, three different mono- or dialkoxy-substituted benzene rings were employed as the donor groups: as mentioned above, they were selected due to their moderate electron-donating ability compared to the common donor groups of DSSC sensitizers (*e. g.* triarylamines, indolines) [65], aiming to obtain compounds with relatively low HOMO energy levels, and thus make electron transfer from the reduced form of the WOC to the oxidized dyes thermodynamically favored. The different number and substitution patterns of alkoxy substituents in compounds **1a-c** were expected to induce changes in the electronic structures of the dyes, allowing to modulate their E_{ox}

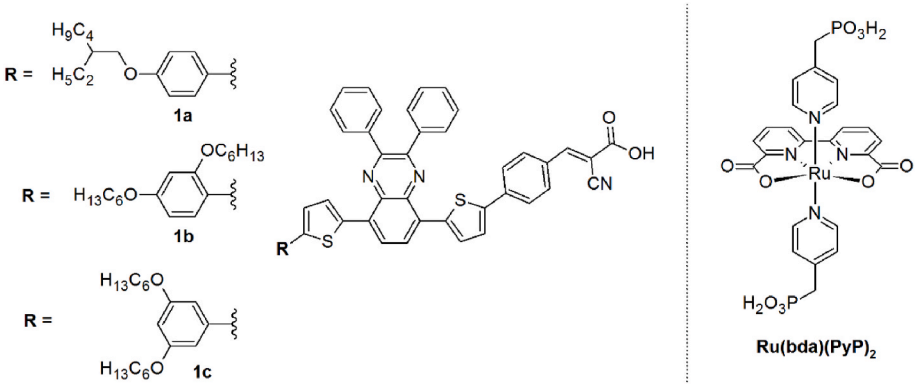

Fig. 2. Structure of organic dyes **1a-c** prepared in this work (left), and of the known water oxidation catalyst **Ru(bda)(PyP)$_2$** (right).

values and therefore evaluate the influence of this parameter on device performances. Finally, the donor groups were decorated with branched or linear alkyl chains to improve the compounds solubility and possibly reduce aggregation upon binding on the semiconductor surface.

In this manuscript, we will present the results of our activity dealing with the modeling, synthesis, characterization and preliminary application in DS-PECs of compounds **1a-c**. First, the dyes structures were assessed computationally by means of DFT and TD-DFT-based methods to model their molecular and electronic properties and simulate their main light-absorption features. Then, the compounds were prepared by application of a concise synthetic sequence featuring Pd-catalyzed direct arylation (DA) reactions as the key C–C bond-forming steps. The dyes were fully characterized from the spectroscopic and electrochemical point of view, both in solution and after adsorption on electrodes made of thin films of nanocrystalline TiO_2, which included the investigation of the charge transfer processes between the dyes and the semiconductor by means of femtosecond Transient Absorption Spectroscopy (TAS) studies.

The known ruthenium complex **Ru(bda)(PyP)$_2$** (Fig. 2; bda = 2,2′-bipyridyl-6,6′-dicarboxylic acid; PyP = pyridin-4-methyl phosphonic acid) [44] was then selected as a water oxidation catalyst to work in combination with dyes **1a-c**, and was prepared by adapting a reported procedure. Finally, photoanodes sensitized with the new dyes and decorated with the chosen WOC were tested in water splitting DS-PEC with a 0.1 M aq. Na_2SO_4 electrolyte, to determine their relative performances.

2. Materials and methods

2.1. General synthetic remarks

All commercially available compounds were purchased from Merck KGaA, Fluorochem Ltd., and T.C.I. Europe Co. Ltd., and were used without further purification unless otherwise stated. In particular, 4,7-dibromobenzo[*c*][1,2,5]thiadiazole (**2**), 2-(tributylstannyl)thiophene (**3**), benzil (**5**), 2,2′-bipyridine-6,6′-dicarboxylic acid (**bda**) and pyridin-4-ylmethylphosphonic acid (**15**) were obtained from the above-mentioned commercial suppliers. 1-Bromo-4-((2-ethylhexyl)oxy)benzene (**9a**) [66], 1-bromo-2,4-bis(hexyloxy)benzene (**9b**) [67], 1-bromo-3,5-bis(hexyloxy)benzene (**9c**) [68] and the complex [Ru(bda)(DMSO)$_2$] [27] were prepared according to the previously published synthetic procedures. Before use, Zn dust was stirred in a 1 M HCl aqueous solution for 15 min, then it was filtered and washed with water, ethanol and diethyl ether, in this order, to remove adventitious traces of zinc oxides. The resulting activated Zn dust was dried under vacuum and could be stored for months under nitrogen atmosphere. Anhydrous toluene, *N*,*N*-dimethylformamide (DMF), tetrahydrofuran (THF), and dichloromethane (DCM) were obtained after drying with a PureSolv Micro apparatus (Inert). Palladium-catalyzed reactions were carried out under a dry nitrogen atmosphere using Schlenk techniques. Reactions were monitored by TLC on Kieselgel 60 F254 (*Merck*) aluminum sheets and the products were visualized by exposing the plate to UV light or by staining it with a basic aqueous potassium permanganate ($KMnO_4$) solution. Flash column chromatography was performed using *Merck* Kieselgel 60 (300–400 mesh) as the stationary phase. ^{1}H NMR spectra were recorded at 200–400 MHz, and ^{13}C NMR spectra were recorded at 50.3–100.6 MHz, respectively, on *Varian* Gemini/Mercury/INOVA instruments. Chemical shifts (δ) are reported in parts per million (ppm) and are referenced to the residual solvent peak ($CDCl_3$, $\delta = 7.26$ ppm for ^{1}H NMR and $\delta = 77.16$ ppm for ^{13}C NMR; CD_2Cl_2, $\delta = 5.32$ ppm for ^{1}H NMR and $\delta = 53.84$ ppm for ^{13}C NMR; THF-*d8*, $\delta = 1.72$, 3.58 ppm for ^{1}H NMR and $\delta = 25.31$, 67.21 ppm for ^{13}C NMR; DMSO-d_6, $\delta = 2.50$ ppm for ^{1}H NMR and $\delta = 39.52$ ppm for ^{13}C NMR; CD_3OD, $\delta = 3.31$ ppm for ^{1}H NMR and $\delta = 49.00$ ppm for ^{13}C NMR). The following abbreviations are used to indicate the multiplicity: s, singlet; d, doublet; t, triplet; q, quartet; m, multiplet; bs, broad signal. ESI-MS spectra were obtained by direct injection of the sample solution using a *Thermo Scientific* LCQ-FLEET instrument, while HRMS spectra were measured using a *Thermo Scientific* LTQ Orbitrap (FT-MS) instrument (carried out at the Interdepartmental Center for Mass Spectroscopy of the University of Florence, CISM); both are reported as *m/z*.

2.2. Synthetic procedures

2.2.1. 4,7-Di(thiophen-2-yl)benzo[c]*[1,2,5]*thiadiazole (4)

4,7-Dibromobenzo[*c*][1,2,5]thiadiazole (**2**, 1.00 g, 3.40 mmol, 1.0 eq.) and $PdCl_2(PPh_3)_2$ (0.047 g, 0.068 mmol, 2.0 mol%) were added to a Schlenk tube and put under inert atmosphere by performing three vacuum-nitrogen cycles. The solids were then dissolved in dry DMF (25 mL) and the solution was stirred for 5 min. Then, 2-(tributylstannyl) thiophene (**3**, 2.79 g, 7.48 mmol, 2.2 eq.) was added via syringe and the reaction was stirred at reflux for 24 h. The reaction mixture was allowed to cool down to room temperature, then water (25 mL) was added, and the mixture was extracted with DCM (3 × 25 mL). The organic phases were combined and dried over anhydrous Na_2SO_4, filtered and the solvent evaporated under reduced pressure. The crude was purified by recrystallization from ethanol to give compound **4** as a bright yellow solid (0.950 g, 3.16 mmol, 93 % yield). ^{1}H NMR (400 MHz, $CDCl_3$) δ = 8.13 (dd, J = 3.7, 1.1 Hz, 2H), 7.89 (s, 2H), 7.46 (dd, J = 5.1, 1.1 Hz, 2H), 7.22 (dd, J = 5.1, 3.7 Hz, 2H) ppm. Spectroscopic data are in agreement with those reported in the literature [69].

2.2.2. 2,3-Diphenyl-5,8-di(thiophen-2-yl)quinoxaline (6)

In a round bottom flask 4,7-di(thiophen-2-yl)benzo[c][1,2,5]thiadiazole (**4**, 0.950 g, 3.16 mmol, 1.0 eq.) and zinc powder (2.07 g, 31.6 mmol, 10 eq.) were suspended in glacial acetic acid (25 mL). The reaction mixture was vigorously stirred at 80 °C for 1.5 h to obtain a complete conversion of the starting material as assessed by TLC (eluent:

petroleum ether/DCM 4:1 v/v). The mixture was then cooled to room temperature and filtered. The filtrate was poured in water and extracted with diethyl ether (3 × 30 mL). The combined organic phases were dried over Na_2SO_4, filtered, and the solvent evaporated under reduced pressure. Without any further purification, the crude mixture was then dissolved in ethanol (20 mL) and benzil (**5**, 0.731 g, 3.48 mmol, 1.1 eq.) was subsequently added. The reaction mixture was then vigorously stirred at 80 °C for 16 h. After cooling down to room temperature, the mixture was filtered through a fritted funnel and the solid residue washed with cold ethanol, to afford compound **6** as a yellow solid (1.30 g, 2.91 mmol, 92 % yield). ^{1}H NMR (400 MHz, $CDCl_3$) δ = 8.16 (s, 2H), 7.89 (dd, J = 3.8, 1.1 Hz, 2H), 7.82–7.71 (m, 4H), 7.53 (dd, J = 5.1, 1.1 Hz, 2H), 7.45–7.37 (m, 6H), 7.19 (dd, J = 5.2, 3.8 Hz, 2H). Spectroscopic data are in agreement with those reported in the literature [70].

2.2.3. 4-(5-(2,3-Diphenyl-8-(thiophen-2-yl)quinoxalin-5-yl)thiophen-2-yl) benzaldehyde (8)

2,3-Diphenyl-5,8-di(thiophen-2-yl)quinoxaline (**6**, 1.00 g, 2.24 mmol, 2.0 eq.), 4-bromobenzaldehyde (**7**, 207 mg, 1.12 mmol, 1.0 eq.), Cs_2CO_3 (2.19 g, 3.36 mmol, 3.0 eq), $Pd(OAc)_2$ (13 mg, 0.056 mmol, 5 mol%), P(2-MeOPh)$_3$ (39 mg, 0.112 mmol, 10 mol%) and pivalic acid (34 mg, 0.336 mmol, 30 mol%) were added to a Schlenk tube and put under inert atmosphere by performing three vacuum-nitrogen cycles. The solids were then dissolved in dry toluene (32 mL) and the reaction mixture was vigorously stirred at 110 °C for 24 h. The solution was cooled to room temperature, diluted with DCM (20 mL), filtered over a pad of Celite®, and washed with water (2 × 30 mL) and brine (30 mL). The organic phase was dried over Na_2SO_4, filtered, and the solvent evaporated under reduced pressure. The crude product was purified by flash column chromatography (SiO_2, gradient from petroleum ether/DCM 3:1 to petroleum ether/DCM 1:1) to afford compound **8** (434 mg, 0.788 mmol, 70 % yield) as a dark yellow solid. ^{1}H NMR (400 MHz, $CDCl_3$) δ = 10.01 (s, 1H), 8.14 (s, 2H), 7.92–7.85 (m, 4H), 7.81 (d, J = 8.0 Hz, 2H), 7.80–7.72 (m, 4H), 7.54 (d, J = 5.1 Hz, 1H), 7.51 (d, J = 4.1 Hz, 1H) 7.48–7.3 (m, 6H), 7.19 (dd, J = 5.1, 3.7 Hz, 1H) ppm. ^{13}C NMR (100 MHz, $CDCl_3$) δ = 191.7, 152.0, 151.8, 145.1, 140.6, 140.3, 138.64, 138.58, 137.3, 137.2, 135.0, 131.8, 130.67, 130.66, 130.61, 129.39, 129.36, 129.27, 128.41, 128.36, 127.60, 127.56, 127.0, 126.8, 126.7, 125.8, 124.9 ppm. MS (ESI) m/z: $[M + H]^+$ calcd for $C_{35}H_{23}N_2OS_2$ 551.1; found: 551.3.

2.2.4. General procedure for the synthesis of compounds 10a-c (GP1)

4-(5-(2,3-Diphenyl-8-(thiophen-2-yl)quinoxalin-5-yl)thiophen-2-yl) benzaldehyde (**8**), the appropriate aryl bromide **9a-c** (3.0 eq.) and Cs_2CO_3 (3.0 eq.) were added to a Schlenk tube and put under inert atmosphere by performing three vacuum-nitrogen cycles. The solids were dissolved in dry toluene (3 mL) and a solution of $Pd(OAc)_2$ (5 mol%), P(2-MeOPh)$_3$ (10 mol%) and pivalic acid (30 mol%) in toluene (1 mL) was added. The reaction mixture was stirred at 110 °C for 24 h. After cooling down to room temperature, water (5 mL) was added and the mixture extracted with DCM (3 × 10 mL). The combined organic phases were dried over anhydrous Na_2SO_4, filtered, and the solvent evaporated under reduced pressure. Crude products were then purified by flash column chromatography to give the desired compounds **10a-c** in pure form.

2.2.5. 4-(5-(8-(5-(4-((2-Ethylhexyl)oxy)phenyl)thiophen-2-yl)-2,3-diphenylquinoxalin-5-yl)thiophen-2-yl)benzaldehyde (10a)

Prepared following general procedure GP1, using 4-(5-(2,3-diphenyl-8-(thiophen-2-yl)quinoxalin-5-yl)thiophen-2-yl)benzaldehyde (**8**) (50 mg, 0.091 mmol, 1.0 eq.), 1-bromo-4-((2-ethylhexyl)oxy)benzene (**9a**, 78 mg, 0.273 mol, 3.0 eq.), Cs_2CO_3 (89 g, 0.273 mmol, 3.0 eq.), $Pd(OAc)_2$ (2 mg, 0.009 mmol, 10 mol%), P(2-MeOPh)$_3$ (6 mg, 0.018 mmol, 20 mol%) and pivalic acid (3 mg, 0.027 mmol, 30 mol%). The crude product was purified by flash column chromatography (SiO_2, petroleum ether/THF 85:15 v/v) to afford compound **10a** as a red solid (55 mg, 0.073 mmol, 80 % yield). ^{1}H NMR (400 MHz, THF-*d8*) δ = 9.95 (s, 1H), 8.27-8.19 (m, 2H), 7.97–7.85 (m, 6H), 7.83–7.75 (m, 4H), 7.65-7.58 (m, 3H), 7.46–7.35 (m, 6H), 7.30 (d, J = 3.9 Hz, 1H), 6.96 (d, J = 8.6 Hz, 2H), 3.92 (d, J = 5.9 Hz, 2H), 1.53 (m, 4H), 1.38 (m, 4H), 1.01–0.90 (m, 6H) ppm. ^{13}C NMR (100 MHz, THF-*d8*) δ = 191.3, 160.4, 152.8, 152.7, 148.7, 146.2, 141.3, 141.0, 139.9, 138.1, 137.6, 136.6, 132.8, 131.7, 131.1, 130.1, 130.0, 129.11, 129.08, 128.8, 128.5, 127.60, 127.55, 127.0, 126.4, 125.7, 122.6, 115.8, 71.3, 40.7, 31.7, 30.2, 25.0, 24.2, 14.6, 11.7 ppm. *Note: not all carbon signals are visible in the ^{13}C-NMR spectrum due to fortuitous overlaps of aromatic peaks*. MS (ESI) m/z: $[M + H]^+$ calcd for $C_{49}H_{43}N_2O_2S_2$ 755.3; found: 755.3.

2.2.6. 4-(5-(8-(5-(2,4-Bis(Hexyloxy)phenyl)thiophen-2-yl)-2,3-diphenylquinoxalin-5-yl)thiophen-2-yl)benzaldehyde (10b)

Prepared following general procedure GP1, using 4-(5-(2,3-Diphenyl-8-(thiophen-2-yl)quinoxalin-5-yl)thiophen-2-yl)benzaldehyde (**8**) (50 mg, 0.091 mmol, 1.0 eq.), 1-bromo-2,4-bis(hexyloxy)benzene (**9b**, 97 mg, 0.273 mmol, 3.0 eq.), Cs_2CO_3 (89 mg, 0.273 mmol, 3.0 eq.), $Pd(OAc)_2$ (2 mg, 0.009 mmol, 10 mol%), P(2-MeOPh)$_3$ (6 mg, 0.018 mmol, 20 mol%) and pivalic acid (3 mg, 0.027 mmol, 30 mol%). The crude product was purified by flash column chromatography (SiO_2, gradient from petroleum ether/DCM 9:1 v/v to petroleum ether/DCM 3:2 v/v) to afford compound **10b** as a red solid (70 mg, 0.085 mmol, 93 % yield). ^{1}H NMR (400 MHz, CD_2Cl_2) δ = 9.96 (s, 1H), 8.11–8.05 (m, 2H), 7.89–7.84 (m, 3H), 7.82–7.72 (m, 7H), 7.59 (d, J = 8.3 Hz, 1H), 7.57–7.48 (m, 2H), 7.46–7.35 (m, 6H), 6.57–6.52 (m, 2H), 4.07 (t, J = 6.6 Hz, 2H), 4.00 (t, J = 6.6 Hz, 2H), 1.81 (m, 4H), 1.55–1.45 (m, 4H), 1.41–1.35 (m, 4H), 1.33–1.29 (m, 4H), 0.94 (t, J = 7.0 Hz, 3H), 0.86 (m, t, J = 7.0 Hz, 3H) ppm. ^{13}C NMR (100 MHz, CD_2Cl_2) δ = 191.2, 160.0, 156.5, 151.6, 151.5, 144.7, 143.3, 140.2, 140.1, 138.7, 137.2, 137.0, 136.7, 135.0, 132.1, 130.5, 130.4, 130.2, 129.7, 129.1, 128.9, 128.8, 128.1, 127.4, 127.1, 126.5, 126.4, 125.4, 124.6, 124.4, 116.2, 105.7, 99.9, 68.8, 68.2, 31.6, 31.5, 29.3, 29.0, 25.8, 25.7, 22.6, 22.5, 13.80, 13.77 ppm. MS (ESI) m/z: $[M + H]^+$ calcd for $C_{53}H_{51}N_2O_3S_2$ 827.3; found: 827.4.

2.2.7. 4-(5-(8-(5-(3,5-Bis(hexyloxy)phenyl)thiophen-2-yl)-2,3-diphenylquinoxalin-5-yl)thiophen-2-yl)benzaldehyde (10c)

Prepared following general procedure GP1, using 4-(5-(2,3-diphenyl-8-(thiophen-2-yl)quinoxalin-5-yl)thiophen-2-yl)benzaldehyde (**8**) (40 mg, 0.073 mmol, 1.0 eq), 1-bromo-3,5-bis(hexyloxy)benzene (**9c**, 78 mg, 0.219 mmol, 3.0 eq), Cs_2CO_3 (71 mg, 0.219 mmol, 3.0 eq), $Pd(OAc)_2$ (2 mg, 0.008 mmol, 10 mol%), P(2-MeOPh)$_3$ (5 mg, 0.015 mmol, 20 mol%) and pivalic acid (2 mg, 0.022 mmol, 30 mol%). The crude product was purified by flash column chromatography (SiO_2, gradient from petroleum ether/DCM 9:1 v/v to petroleum ether/DCM 3:2 v/v) to afford compound **10c** as a red solid (56 mg, 0.068 mmol, 93 % yield). ^{1}H NMR (400 MHz, $CDCl_3$) δ = 9.99 (s, 1H), 8.07 (br s, 2H), 7.88 (d, J = 8.1 Hz, 2H), 7.83–7.73 (m, 8H), 7.49–7.32 (m, 8H), 6.85-6.81 (m, 2H), 6.43 (s, 1H), 4.00 (t, J = 6.5 Hz, 4H), 1.88–1.76 (m, 4H), 1.56–1.45 (m, 4H), 1.43–1.32 (m, 8H), 0.94 (t, J = 6.7 Hz, 6H) ppm. ^{13}C NMR (100 MHz, $CDCl_3$) δ = 191.6, 160.8, 151.79, 151.77, 147.7, 145.1, 140.6, 140.3, 138.7, 137.8, 137.2, 136.4, 135.1, 131.7, 130.8, 130.7, 130.6, 130.4, 129.4, 129.2, 128.4, 128.3, 127.6, 126.7, 126.3, 125.7, 124.9, 123.2, 104.5, 101.0, 68.3, 31.8, 29.5, 26.0, 22.8, 14.2 ppm. *Note: not all carbon signals are visible in the ^{13}C-NMR spectrum due to fortuitous overlaps of aromatic peaks*. MS (ESI) m/z: $[M + H]^+$ calcd for $C_{53}H_{51}N_2O_3S_2$ 827.3; found: 827.4.

2.2.8. General procedure for the synthesis of compounds 1a-c (GP2)

The appropriate aldehyde **10a-c** was added to a Schlenk tube, put under inert atmosphere by performing three vacuum-nitrogen cycles and dissolved in a mixture of $CHCl_3/CH_3CN$ 3:2 v/v (10 mL). Cyanoacetic acid (**11**, 10 eq.) and piperidine (0.3 eq.) were then added and the reaction mixture was stirred at 90 °C for 16 h. After cooling down to room temperature, water (5 mL) was added and the mixture was

extracted with DCM (3 × 10 mL). The combined organic phases were dried over anhydrous Na_2SO_4, filtered, and the solvent evaporated under reduced pressure. The crude mixture was washed several times with cold ethanol to give the corresponding compounds **1a-c**.

2.2.9. 3-(4-(5-(8-(5-(4-((2-Ethylhexyl)oxy)phenyl)thiophen-2-yl)-2,3-diphenylquinoxalin-5-yl)thiophen-2-yl)phenyl)-2-cyanoacrylic acid (1a)

Prepared following general procedure GP2, using 4-(5-(8-(5-(4-((2-ethylhexyloxy)phenyl)tiophen-2-yl)-2,3-diphenylquinoxaline-5-yl)tiophen-2-yl)benzaldehyde (**10a**, 55 mg, 0.073 mmol, 1.0 eq.), cyanoacetic acid (60 mg, 0.715 mmol, 10 eq.) and piperidine (2 mg, 0.022 mmol, 0.3 eq.). The crude mixture was washed several times with cold ethanol to afford compound **1a** as a red solid (49 mg, 0.060 mmol, 82 % yield). ^{1}H NMR (400 MHz, THF-*d8*) δ = 8.27–8.19 (m, 3H), 8.09 (d, J = 8.4 Hz, 2H), 7.95 (d, J = 4.0 Hz, 1H), 7.92 (d, J = 3.9 Hz, 1H), 7.85 (d, J = 8.4 Hz, 2H), 7.84–7.76 (m, 5H), 7.67–7.56 (m, 3H), 7.47–7.36 (m, 7H), 7.31 (d, J = 3.9 Hz, 1H), 6.96 (d, J = 8.7 Hz, 2H), 3.95–3.90 (m, 2H), 1.63–1.44 (m, 4H), 1.43–1.32 (m, 4H), 1.01–0.90 (m, 6H) ppm. ^{13}C NMR (100 MHz, THF-*d8*) δ = 164.1, 160.4, 153.9, 152.8, 152.7, 148.7, 146.2, 141.1, 140.2, 139.9, 138.1, 137.7, 132.8, 131.7, 131.2, 130.1, 130.0, 129.2, 129.1, 128.8, 128.6, 128.5, 127.6, 127.3, 127.0, 126.5, 125.9, 122.6, 121.8, 116.7, 115.9, 112.8, 103.6, 71.3, 40.7, 31.7, 30.8, 30.2, 24.1, 14.6, 11.7 ppm. *not all carbon signals are visible in the ^{13}C-NMR spectrum due to fortuitous overlaps of aromatic peaks*. HRMS (ESI) *m/z*: $[M+H]^+$ calcd for $C_{52}H_{44}N_3O_3S_2$ 822.2819; found 822.2821.

2.2.10. 3-(4-(5-(8-(5-(2,4-Bis(hexyloxy)phenyl)thiophen-2-yl)-2,3-diphenylquinoxalin-5-yl)thiophen-2-yl)phenyl)-2-cyanoacrylic acid (1b)

Prepared following general procedure GP2, using 4-(5-(8-(5-(2,4-bis(hexyloxy)phenyl)tiophen-2-yl)-2,3-diphenylquinoxalin-5-yl)tiophen-2-yl)benzaldehyde (**10b**, 70 mg, 0.085 mmol, 1.0 eq.), cyanoacetic acid (72 mg, 0.846 mmol, 10 eq.) and piperidine (2 mg, 0.025 mmol, 0.3 eq.). The crude mixture was washed several times with cold ethanol to afford compound **1b** as a red solid (62 mg, 0.069 mmol, 82 % yield). ^{1}H NMR (400 MHz, THF-*d8*) δ = 8.32–8.20 (m, 3H), 8.11 (d, J = 8.2 Hz, 2H), 8.00–7.96 (m, 2H), 7.88 (d, J = 8.1 Hz, 2H), 7.84–7.77 (m, 4H), 7.67–7.61 (m, 2H), 7.53 (d, J = 4.0 Hz, 1H), 7.45–7.36 (m, 7H), 6.62 (d, J = 2.5 Hz, 1H), 6.56 (dd, J = 8.5, 2.4 Hz, 1H), 4.09 (t, J = 6.5 Hz, 2H), 4.01 (t, J = 6.4 Hz, 2H), 1.83–1.76 (m, 4H), 1.55–1.46 (m, 4H), 1.42–1.35 (m, 4H), 1.33–1.26 (m, 4H), 0.97–0.91 (m, 3H), 0.88–0.82 (m, 3H) ppm. ^{13}C NMR (100 MHz, THF-*d8*) δ = 164.1, 161.2, 157.7, 153.9, 152.76, 152.75, 146.1, 144.8, 141.3, 140.3, 140.1, 140.0, 138.4, 138.2, 137.7, 133.5, 132.8, 131.8, 131.7, 130.9, 130.1, 129.9, 129.7, 129.14, 129.08, 128.5, 128.3, 127.8, 127.3, 126.5, 125.9, 125.2, 117.6, 116.7, 111.7, 106.8, 103.6, 101.1, 69.7, 68.8, 32.8, 32.7, 30.5, 30.2, 27.0, 26.9, 23.7, 23.6, 14.6, 14.6 ppm. HRMS (ESI) *m/z*: $[M+H]^+$ calcd for $C_{56}H_{52}N_3O_4S_2$ 894.3394; found 894.3391.

2.2.11. 3-(4-(5-(8-(5-(3,5-Bis(hexyloxy)phenyl)thiophen-2-yl)-2,3-diphenylquinoxalin-5-yl)thiophen-2-yl)phenyl)-2-cyanoacrylic acid (1c)

Prepared following general procedure GP2, using 4-(5-(8-(5-(3,5-*bis*(hexyloxy)phenyl)thiophen-2-yl)-2,3-diphenylquinoxalin-5-yl)thiophen-2-yl)benzaldehyde (**10c**, 56 mg, 0.068 mmol, 1.0 eq.), cyanoacetic acid (58 mg, 0.677 mmol, 10 eq.) and piperidine (2 mg, 0.020 mmol, 0.3 eq.). The crude mixture was washed several times with cold ethanol to afford compound **1c** as a red solid (54 mg, 0.060 mmol, 89 % yield). ^{1}H NMR (400 MHz, THF-*d8*) δ = 8.28 (s, 2H), 8.23 (s, 1H), 8.10 (d, J = 8.5 Hz, 2H), 7.99 (d, J = 4.0 Hz, 1H), 7.95 (d, J = 4.0 Hz, 1H), 7.87 (d, J = 8.4 Hz, 2H), 7.86–7.79 (m, 5H), 7.64 (d, J = 4.0 Hz, 1H), 7.48–7.37 (m, 7H), 6.87 (d, J = 2.1 Hz, 2H), 6.42 (t, J = 2.1 Hz, 1H), 4.02 (t, J = 6.4 Hz, 4H), 1.84–1.79 (m, 4H), 1.59–1.50 (m, 4H), 1.41 (m, 8H), 0.99–0.92 (m, 6H) ppm. ^{13}C NMR (100 MHz, THF-*d8*) δ = 164.1, 161.9, 153.9, 152.9, 152.8, 148.8, 146.3, 141.0, 140.2, 139.9, 139.8, 138.4, 138.1, 138.0, 137.3, 132.8, 132.5, 131.8, 131.7, 131.4, 130.2, 130.0, 129.2, 129.1, 128.7, 128.4, 127.6, 127.1, 126.5, 125.9, 123.8, 116.7, 104.8, 103.5, 101.7, 96.2, 68.8, 32.8, 30.5, 27.0, 24.0, 14.6 ppm. HRMS (ESI) *m/z*: $[M+H]^+$ calcd for $C_{56}H_{52}N_3O_4S_2$ 894.3394; found 894.3398.

2.2.12. [Ru(bda)(DMSO)$_2$] (12)

2,2′-bipyridine-6,6′-dicarboxylic acid (**bda**, 350 mg, 0.722 mmol, 1.0 eq.) and $[Ru(DMSO)_4Cl_2]$ (176 mg, 0.722 mmol, 1.0 eq.) were added to a Schlenk tube and put under inert atmosphere by performing three vacuum-nitrogen cycles. The solids were then suspended in dry methanol (15 mL) and the solution degassed by bubbling N_2 for 15 min. Et_3N (439 mg, 4.33 mmol, 6.0 eq.) was then added, and the mixture was heated up and stirred under reflux for 4 h. After cooling to room temperature, the reaction mixture was centrifuged (4000 rpm, 10 min, rt). The resulting precipitate was then washed with cold methanol to afford the desired product as a dark brown solid (251 mg, 0.502 mmol, 70 % yield). ^{1}H NMR (400 MHz, DMSO-d_6) δ = 8.64 (d, J = 8.0 Hz, 2H), 8.14 (t, J = 7.9 Hz, 2H), 8.02 (d, J = 7.8 Hz, 2H), 2.52 (s, 6H) ppm. Spectroscopic data are in agreement with those reported in the literature [27].

2.2.13. [Ru(bda)(PyP)$_2$]

$[Ru(bda)(DMSO)_2]$ (117 mg, 0.234 mmol, 1.0 eq.) was added to a Schlenk tube, put under inert atmosphere by performing three vacuum-nitrogen cycles, and suspended in dry methanol (10 mL). The mixture was degassed by bubbling N_2 for 15 min and heated at 60 °C. Then a solution of (pyridin-4-ylmethyl)phosphonic acid (**15**, 89 mg, 0.515 mmol, 2.2 eq.) in a 1,1,1,3,3,3-hexafluoro-2-propanol (HFIP)/methanol 1:4 (5 mL) mixture, previously prepared in another Schlenk tube under inert atmosphere and pre-heated at 60 °C, was added via a gas-tight syringe. The reaction mixture was vigorously stirred at 80 °C for 16 h. After cooling to room temperature, the volume of the solvent was reduced to ca. 8 mL. The mixture was centrifuged (4000 rpm, 10 min, rt). The resulting solid was washed with DCM and methanol, to afford the desired product as dark brown solid (110 mg, 0.200 mmol, 68 % yield). *Note: due to partial oxidation under air, with consequent formation of less soluble paramagnetic species, NMR spectra of the catalyst were recorded in the presence of a small amount of hydroquinone as a reducing agent*. ^{1}H NMR (400 MHz, CD_3OD + Hydroquinone) δ 8.55 (dd, J = 8.0, 1.1 Hz, 2H), 8.01 (d, J = 7.7 Hz, 2H), 7.87 (t, J = 7.9 Hz, 2H), 7.71 (d, J = 6.0 Hz, 4H), 7.14 (dd, J = 6.6, 2.3 Hz, 4H), 3.04 (d, J = 22.5 Hz, 4H) ppm. ^{31}P NMR (162 MHz, CD_3OD + Hydroquinone) δ = 17.50 ppm. MS (ESI) *m/z*: $[M]^+$ calcd for $C_{24}H_{22}N_4O_{10}P_2Ru$ 690.0; found: 689.8.

2.3. Spectroscopic characterization

UV–Vis spectra in different solvents were measured on diluted solutions of the compounds (approx. 10^{-5} M) either with a *Shimadzu* UV-2600 or a *PerkinElmer* Lambda 950 UV–vis–NIR spectrometer. UV–Vis absorption spectra of the same compounds adsorbed on TiO_2 were recorded with a *Shimadzu* UV-2600 spectrometer in transmission mode after the sensitization of thin, transparent semiconductor films (thickness approx. 5 μm, for details on their preparation *see below*, section 2.5). Steady state fluorescence emission and excitation spectra of the dyes at room temperature were obtained either with a *Jasco* FP-8300 or a *Hamamatsu* Edinburgh FLS920 spectrofluorometer. Excitation and emission spectra of the compounds in a frozen MeOH/DCM 1:1 matrix at 77 K were obtained with the same Edinburgh FLS920 spectrofluorometer, using quartz tubes dipped in liquid nitrogen in a quartz Dewar as sample containers.

Time-correlated single photon counting (TCSPC) experiments for the determination of the excited state lifetimes were carried out with an IBH time-correlated single-photon counting apparatus with nanoLED excitation source at 375 nm.

Pump-probe transient absorption measurements on the dyes and catalyst adsorbed on TiO_2 films were performed with an *Ultrafast Systems* HELIOS (HE-VIS-NIR) femtosecond transient absorption spectrometer by using, as excitation source, a *Newport* Spectra Physics Solstice-F-1K-230 V laser system, combined with a TOPAS Prime (TPR-

TOPAS-F) optical parametric amplifier (pulse width: 100 fs, 1 kHz repetition rate) tuned at 500 nm. The pump energy on the sample was 3 μJ/pulse. Probe beams with a generated continuum both in the visible range (450–800 nm) and in the NIR range (800–1600 nm) have been employed and the spectra have been merged in the analysis. The overall time resolution of the system is 300 fs. Surface Xplorer V4 software from *Ultrafast Systems* was used for data acquisition and analysis. The 3D data surfaces were corrected for the chirp of the probe pulse prior to analysis. The estimated error on transient absorbance lifetimes is 10 %.

2.4. Electrochemical and spectroelectrochemical characterization

Cyclic voltammetries (CV) of the dyes in DCM solution were recorded with an *Agilent* B2901 precision SMU using a glassy carbon electrode as the working electrode, a platinum wire as the counter electrode, and an $Ag/AgNO_3$ (0.01 M in CH_3CN) pseudo-reference electrode. 0.1 M $TBAPF_6$ was used as the supporting electrolyte, with a scan speed of 100 mV s^{-1}. Curves were recorded first in the absence and then in the presence of ferrocene (Fc), used as an internal standard. The E_{ox} of the compounds were referenced to that of the $Fc^{+/0}$ couple, and the latter was used to set the potential scale assuming its redox potential to be equal to 0.72 V *vs.* NHE in DCM, according to the literature [71].

CVs of the FTO/TiO_2/**dye** + **Ru(bda)(PyP)$_2$** electrodes (for details on their preparation *see below*, section 2.5), employed as working electrodes, were recorded with a *Metrohm Autolab* PGSTAT 302N + FRA32M electrochemical workstation, using a Saturated Calomel Electrode (SCE) as the reference electrode and a platinum wire as the counter electrode, and the data were recorded and elaborated by Nova 1.6 software. Measurements were performed in a 0.1 M phosphate buffer solution (pH = 6.6), between −0.05 V and +1.4 V *vs.* SCE at scan rate of 50 mV s^{-1} (3 cycles). Prior to each measurement, electrolytic solutions were degassed with argon for 10 min.

The *in situ* UV–vis–NIR spectroelectrochemical measurements were carried out with a *Metrohm Autolab* PGSTAT204 potentiostat/galvanostat and a *PerkinElmer* Lambda 950 spectrophotometer in a thin layer quartz glass spectroelectrochemical cell (*ALS*, model SEC-C). A platinum gauze was used as the working electrode, a platinum wire was the counterelectrode while the reference electrode was made by Ag/Ag^+ in $AgNO_3$ 0.01 M in acetonitrile (*ALS*, model RE-7). Tetrabutylammonium hexafluophosphate ($TBAPF_6$) 0.1 M in dichloromethane was used as the electrolyte. All the solutions were deaerated for 15 min in argon and the cuvette was sealed for maintaining the argon atmosphere during the experiments. The spectroelectrochemical tests were carried out at room temperature.

2.5. Photolectrode preparation and staining procedure

10 × 10 cm FTO-coated conducting glass sheets (TEC 8 Ω sq^{-1}, GreatCell solar) were cleaned in an ultrasonic bath by the following procedure: (a) immersion in soapy water (15′), followed by rinsing with demineralized water (3 ×); (b) immersion in demineralized water (15′), followed by rinsing with acetone (3 ×); (c) immersion in acetone (15’). The sheets were then immersed for 10 s in boiling *iso*-propanol, followed by drying.

The mesoporous TiO_2 layer was deposited on the FTO glass by printing a single layer of a commercially available nanocrystalline TiO_2 paste (DyeSol TiO_2 Paste DSL 18NR-T, mechanically stirred for 20′ prior to use) in 1.0 × 1.0 cm^2 spots, using an *Aurel* C920 semi-automatic screen printer. The plates were left to sit in an EtOH-fumes-filled chamber for 30” before drying at 120 °C for 30 min, then sintered according to the following programmed ramp: 15′ at 350 °C, 30’ at 375 °C, 1 h at 450 °C, and 1 h at 500 °C. The active area of the resulting mesoporous semi-transparent TiO_2 films was 1.0 cm^2 and the plates were cut into 2.5 × 2.5 cm^2 slides.

For the preparation of the co-adsorption staining solutions, dyes **1a-c** were first dissolved in the appropriate volume of anhydrous and degassed THF, then the same volume of anhydrous and degassed MeOH was added to obtain 4×10^{-4} M solutions of the dyes in a THF/MeOH 1:1 (v/v) mixture. In another container, **Ru(bda)(PyP)$_2$** was dissolved in a small amount of HFIP, and then anhydrous and degassed MeOH was added to obtain a 2×10^{-4} M solution of the catalyst in a MeOH/HFIP 9:1 (v/v) mixture. Finally, the dye and catalyst individual solutions were mixed in a 1:1 ratio to obtain the desired co-adsorption staining solution, with concentrations of 2×10^{-4} M (dye) and 1×10^{-4} M (catalyst) in a MeOH/THF/HFIP 70:25:5 (v/v) mixture. The staining solutions for the sequential procedure were instead obtained by simply diluting to double volume the above-mentioned individual dye (**1b**) and catalyst solutions, obtaining the same final concentrations of 2×10^{-4} M (dye) and 1×10^{-4} M (catalyst).

The slides with the printed TiO_2 films were heated on a hot plate at 80 °C for at least 1 h. For the co-adsorption procedure, while still warm, they were then immersed in the appropriate combined **1a-c** + **Ru(bda)(PyP)$_2$** solution for 4 h, after which the electrodes were rinsed with ethanol and dried under airflow. For the sequential adsorption procedure, they were instead immersed first, when still warm, in the **Ru(bda)(PyP)$_2$** solution for 4 h, followed by rinsing with ethanol and immersion in the **1b** solution for another 4h; finally, also in this case they were rinsed with ethanol and dried under airflow.

2.6. Photoelectrochemical measurements

The photoelectrochemical tests were conducted in a three-electrode cell setup with a *Metrohm* Autolab PGSTAT 302 N + FRA32 M electrochemical workstation, using the dye-sensitized and catalyst-functionalized electrodes as working electrodes, an Ag/AgCl/KCl (3 M) reference electrode and a platinum wire as the counter electrode, and the data were recorded and elaborated by Nova 1.6 software. The electrolyte was constituted by a 0.1 M Na_2SO_4 (Sigma Aldrich, ≥99.9 %) solution in demineralized water (pH = 6.5), which was degassed for 10’ with Ar prior to each measurement. The working electrode was illuminated with simulated solar radiation (100 mW cm^{-2} AM 1.5) obtained using a *LOT-ORIEL* Solar Simulator, calibrated with a reference silicon solar cell. A mask was placed on the working electrode so that the illuminated area was 0.5 cm^2. Linear sweep voltammetry (LSV) measurements were conducted under chopped illumination, scanning potentials from −0.5 to +1.3 V *vs.* Ag/AgCl (in the oxidation direction), with a scan rate of 50 mV s^{-1}. Potentials were then referenced to NHE according to the following equation: $E_{NHE} = E_{Ag/AgCl} + 0.2$ V. Chronoamperometry (CA) measurements were conducted for 100 s under the same illumination conditions, measuring the current produced by the cells at a fixed potential of +0.3 V *vs.* Ag/AgCl.

3. Results and discussion

3.1. Computational study of compounds 1a-c

Our work began by modeling the electronic and spectroscopic properties of compounds **1a-c** (Fig. 2) by means of computational methods based on density functional theory (DFT) [72,73] and time-dependent DFT (TD-DFT) [74,75], using Gaussian 16, Revision C.01 suite of programs [76]. In the calculations, the alkyl groups on the donor sections of the molecules were replaced with methyl groups to reduce the computational cost. First of all, the structures of the compounds in the singlet ground state (S_0) were minimized in vacuum at the B3LYP/6-31G* level (Fig. S1, Supporting Information). Clearly, the structures of all compounds appear similar and sufficiently planar, with dihedral angles comprised between approx. 11.0° and 26.5°, allowing to maintain a proper conjugation along the entire molecular scaffold.

Subsequently, B3LYP/6-31G* single-point calculations at ground-state optimized geometries were carried out to obtain the distribution and energy of the respective frontier molecular orbitals (FMOs), including the effects of the chosen solvent, dichloromethane (DCM), by

using the polarizable continuum model (PCM) (Fig. 3) [77]. Considering the FMOs isodensity plots, it can be noticed that for all three compounds the highest occupied molecular orbitals (HOMO) were mainly localized on the donor part of the molecules, with a sizeable contribution from the intermediate quinoxaline ring. Conversely, the lowest unoccupied molecular orbitals (LUMO) were located for the most part on the acceptor cyanoacrylic group, with a smaller contribution coming from the central bridging unit. In general, the computed spatial distribution of the orbitals indicated the existence of a good degree of intramolecular charge transfer (ICT) upon photoexcitation. Furthermore, the evident overlap between the orbitals suggested that the HOMO-LUMO transition could be accompanied by intense light absorption. In terms of computed orbital energies, the LUMOs of all three dyes had similar positions, reflecting the presence of the same acceptor/anchoring group. Compared to **1a**, the HOMO of dye **1b** was instead destabilized by approximately 0.1 eV, as a result of the presence of an additional electrondonating alkoxy group in conjugated position with its unsaturated backbone. On the contrary, the HOMO of compound **1c**, featuring two alkoxy group in *meta*-position, was stabilized by approximately the same extent. As a consequence, the smallest HOMO-LUMO energy difference was displayed by compound **1b**, followed by **1a** and **1c**.

TD-DFT calculations were then employed to assess the spectroscopic properties of the compounds, once again in DCM solution. The fundamental properties investigated were the maximum absorption wavelength (λ_{max}^{abs}), the vertical excitation energy (E_{exc}), the oscillator strength (f) and the percentage composition of the transition in terms of molecular orbitals. They were calculated at the TD-CAM-B3LYP [78]/6-311+G(2d,p) and TD-MPW1K [79]/6-311+G(2d,p) levels of theory, including the solvent effect by means of PCM. The results are reported in Table 1.

As it can be noticed, all compounds present a main transition in the visible region, in the 486–526 nm (2.55–2.36 eV) range, depending on the functional used (for a comparison with experimental values, *see below*). The most red-shifted absorption was exhibited by compound **1b**, owing to its stronger donor group with two alkoxy chains in 2- and 4-position, while the weaker electron-donating capacity of the *bis-meta*-substituted ring of **1c** was evidenced by its slightly blue-shifted transitions. In all cases, the oscillator strengths are high, suggesting a strong light absorption capability, and the corresponding bands are found to stem mostly from HOMO → LUMO transitions, confirming their ICT character.

Based on the above computational investigation, compounds **1a-c** were anticipated to have the appropriate electronic and spectroscopic properties for employment in photoelectrochemical cells, and therefore their preparation was investigated.

Table 1
TD-DFT absorption maxima (λ_{max}^{abs} in nm), excitation energies (E_{exc} in eV), oscillator strengths (f) and contributions (%) to the $S_0 \rightarrow S_1$ transition in DCM of compounds **1a-c**.

Dye	TD-CAM-B3LYP				MPW1K			
	λ_{max}^{abs}	E_{exc}	f	Comp. (%)	λ_{max}^{abs}	E_{exc}	f	Comp. (%)
1a	493	2.52	1.80	69 (H → L)	519	2.39	1.79	80 (H → L)
1b	498	2.49	1.80	66 (H → L)	526	2.36	1.78	78 (H → L)
1c	486	2.55	1.77	75 (H → L)	509	2.43	1.78	83 (H → L)

3.2. Synthesis of compounds 1a-c

The synthetic route followed to obtain common intermediate **8** needed for the preparation of dyes **1a-c** is presented in Scheme 1. The starting material was the commercially available 4,7-dibromo-2,1,3-benzothiadiazole (**2**). By subjecting this compound to a Stille-Migita reaction with tri-*n*-butyl(2-thienyl)stannane (**3**) in the presence of Pd$(PPh_3)_2Cl_2$ as the catalyst, *bis*-thiophen-2-yl derivative **4** could be obtained in high yield. The benzothiadiazole ring of compound **4** was then converted to a quinoxaline system by means of a reduction with elemental zinc in acetic acid, followed by trapping of the resulting diamine with 1,2-diphenylethane-1,2-dione (benzil, **5**) in ethanol, providing the desired compound **6** in 92 % yield. At this stage, insertion of the acceptor portion of the final sensitizers was achieved through a direct arylation reaction [80] of compound **6** with 4-bromobenzaldehyde **7**, in the presence of a palladium complex as the catalyst. To maximize the yield of key intermediate **8**, a short optimization of the reaction protocol was carried out, varying the nature of the phosphine ligand and the base (see Table S1). The best conditions turned out to be the following: $Pd(OAc)_2$ (5 mol%), $P(2\text{-}MeOPh)_3$ (10 mol%), Cs_2CO_3 (3.0 eq.), pivalic acid (30 mol%) in toluene at 110 °C for 24 h. Under such conditions, the desired product could be obtained in 73 % yield on a small scale reaction (0.27 mmol of quinoxaline **6**), which was essentially maintained at 70 % when scaling up to 2.24 mmol of substrate, demonstrating the robustness of the protocol. Importantly, most of the unreacted compound **6** could be recovered after product purification by flash column chromatography, and the reaction time could be also decreased to 1.5 h, albeit at the cost of a slightly reduced yield (67 %).

The synthesis of sensitizers **1a-c** from aldehyde **8** was then

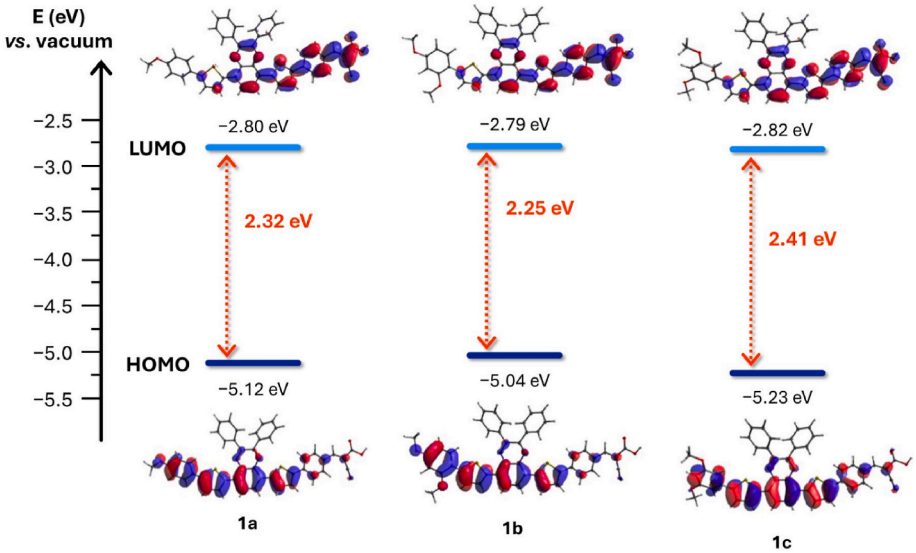

Fig. 3. Energies and electron density spatial distributions of the FMOs of dyes **1a-c** in DCM solution.

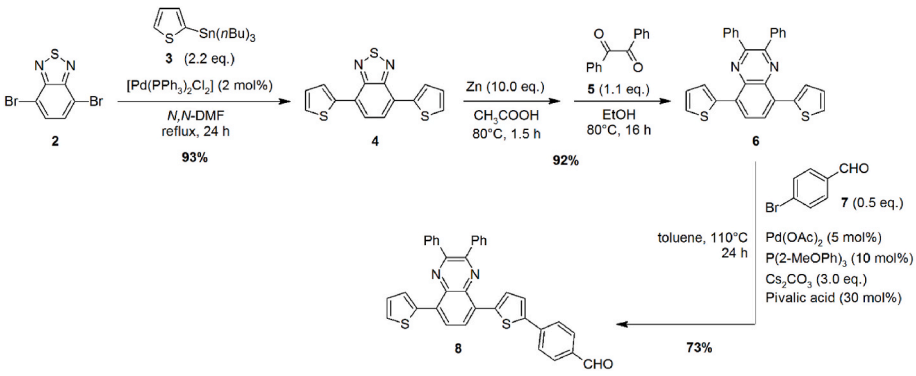

Scheme 1. Synthesis of key common intermediate **8**.

completed through a two-step sequence featuring a second direct arylation step, this time to install the appropriate donor groups, followed by a typical Knoevenagel condensation to insert the cyanoacrylic anchoring group (Scheme 2). Obviously, in order to obtain the three final products, intermediate **8** had to be reacted with each of the three arylbromides **9a-c**, bearing a different number of alkoxy-substituents (one or two) arranged in different substitution patterns. The reactions proceeded under similar conditions to those employed for the coupling between compounds **6** and **7**, allowing to isolate advanced intermediates **10a-c** in 80–93 % yield, where the lower yield of aldehyde **10a** was mostly due to its lower solubility, and thus more difficult handling, compared to **10b, c**. Finally, the desired dyes **1a-c** were obtained in good yields (82–89 %) by condensation of aldehydes **10a-c** with cyanoacetic acid in the presence of a catalytic amount of piperidine; it should be noted that the final compounds could not be purified using flash column chromatography, due to the interaction of the anchoring group with the silica stationary phase, and therefore were isolated by means of recrystallization from ethanol.

3.3. Spectroscopic and electrochemical characterization of dyes 1a-c

The absorption and fluorescence emission spectra of compounds **1a-c** were recorded at room temperature in DCM (Fig. 4, top) and tetrahydrofuran (THF, Fig. 4, bottom) solution, and their main features are listed in Table 2. As expected from the structural design of the dyes, they all exhibited intense light absorption in the visible region, with maxima (λ_{max}^{abs}) comprised approximately in the 490–505 nm range and molar attenuation coefficients (ε) around 2-3 × 10^4 M^{-1} cm^{-1}, typical values for organic donor-acceptor dyes. By comparison of the experimental values with those stemming from the TD-DFT calculations (*see above*), the absorption bands were assigned to transitions involving the frontier molecular orbitals. It can also be seen that a very good agreement with the experimental data was obtained when using the CAM-B3LYP functional for calculations (Table 1), with differences between the computational and experimental E_{exc} values lower than 0.1 eV in all cases. In addition, all dyes presented additional absorption bands of slightly higher intensity in the UV region around 330–345 nm, which were assigned to localized π-π* transitions.

The dyes exhibited a notable fluorescence emission in solution, with maxima in the 610–646 nm range and quantum yields (FQY) comprised between 0.31 and 0.54 in THF (see Table S2). The results obtained in the two solvents were very similar for all dyes: nevertheless, while the absorption maxima did not change much in passing from DCM to THF, a significant red-shift (7–18 nm) was observed for the emission profiles of

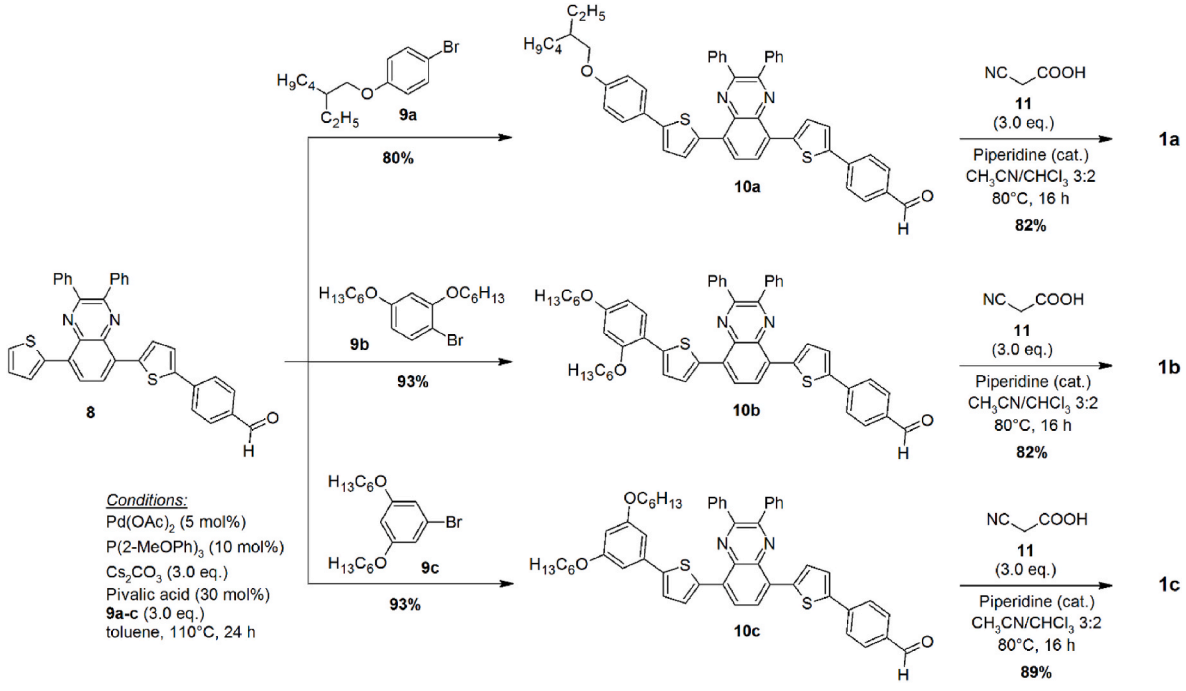

Scheme 2. Final steps of the synthetic route and preparation of sensitizers **1a-c**.

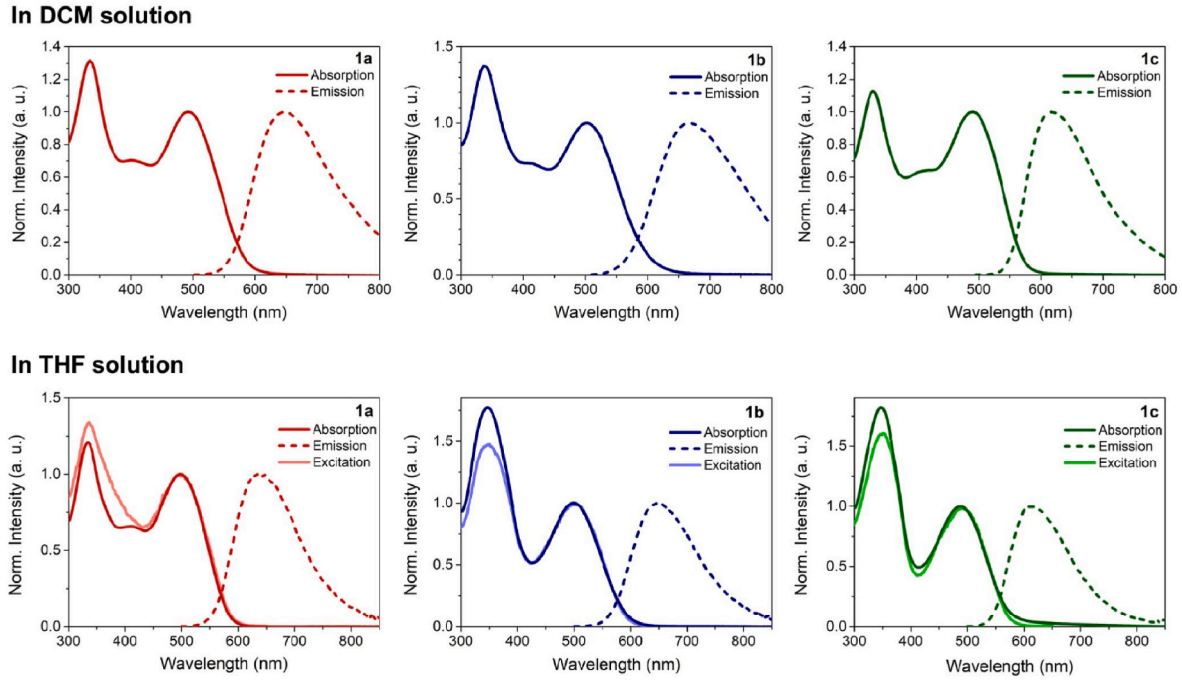

Fig. 4. UV–Vis absorption, emission and excitation spectra of dyes **1a-c** in DCM (top) and THF (bottom) solution at room temperature.

Table 2
Main spectroscopic and electrochemical properties of dyes **1a-c** in DCM and THF solution.

Dye	Solvent	λ^{abs}_{max} (nm)	$\varepsilon \times 10^4$ (M^{-1} cm^{-1})	λ^{emi}_{max} (nm)	$E_{0\text{-}0}$ (eV)[a]	E_{ox} (V) *vs.* Fc^+/Fc	E_{ox} (V) *vs.* NHE[b]	E^*_{ox} (V) *vs.* NHE[c]
1a	DCM	492	2.39	647	2.17	+0.47	+1.19	−0.98
		334	3.14					
	THF	498	3.36	632	2.18	–	–	–
		334	4.05					
1b	DCM	503	2.27	664	2.14	+0.36	+1.08	−1.06
		337	3.11					
	THF	499	1.93	646	2.15	–	–	–
		347	3.42					
1c	DCM	490	2.72	617	2.22	+0.61	+1.33	−0.89
		330	3.07					
	THF	488	2.62	610	2.23	–	–	–
		347	4.77					

[a] Estimated based on the intersection of the normalized absorption and emission spectra.
[b] Calculated by adding +0.72 V to the potential *vs.* Fc^+/Fc [71].
[c] Calculated from the E_{ox} and $E_{0\text{-}0}$ values according to the formula: $E^*_{ox} = E_{ox} - (E_{0\text{-}0}/e)$.

the dyes in the more polar dichloromethane. Furthermore, excitation spectra were also measured for all dyes in THF solution (Fig. 4, bottom). The corresponding excitation profiles, monitored at the maximum emission wavelength, followed those of the corresponding absorption spectra, indicating that, regardless the excitation energy, emission always occurred from the lowest singlet excited state (S_1), according to Kasha's rule. From the intersection of the normalized absorption and emission spectra, the corresponding energies of the $S_0 \rightarrow S_1$ zero-zero transition ($E_{0\text{-}0}$) could be determined, yielding values in the 2.14–2.23 eV range. It can be noted that the largest value of Stokes' shift (approx. 0.5–0.6 eV, 4100-4900 cm^{-1}) and smaller $E_{0\text{-}0}$ were shown by compound **1b**, probably owing to its stronger donor group compared to the other two compounds, and therefore to its more pronounced donor-acceptor character.

Subsequently, to gain further insight into the electronic structures of the dyes and the properties of their excited states, additional fluorescence studies, both under stationary and time-dependent conditions, were carried out in THF solution and in a DCM:MeOH 1:1 frozen matrix at 77K. The results of these supplementary experiments are described in detail in the Supporting Information. In short, all dyes showed similar fluorescence lifetimes and radiative constants, with differences in FQY arising only from the different rates of non-radiative deactivation processes. In addition, emission spectra recorded in glassy solvent at 77 K were slightly blue-shifted with respect to those observed in solution at room temperature, as expected for a CT excited state. The optical band gaps estimated from the emission maxima at 77 K were almost coincident for all three dyes **1a-c** and in the order of 2.1 eV, confirming the similar nature of their excited states.

The characterization of the dyes in solution continued by measuring their ground-state oxidation potentials (E_{ox}) by means of cyclic voltammetry (CV) experiments, using 0.1 M $TBAPF_6$ in DCM as the supporting electrolyte and the ferrocenium/ferrocene redox couple as an internal standard (Fig. 5).

Compounds **1a-c** exhibited quasi-reversible first oxidation waves, which were followed by a second oxidation at more positive potentials. After conversion according to literature reports [71], their E_{ox} values resulted +1.19 V (**1a**), +1.08 V (**1b**) and +1.33 V (**1c**) *vs.* NHE, respectively (Table 2). As it could be expected, the trend observed in the

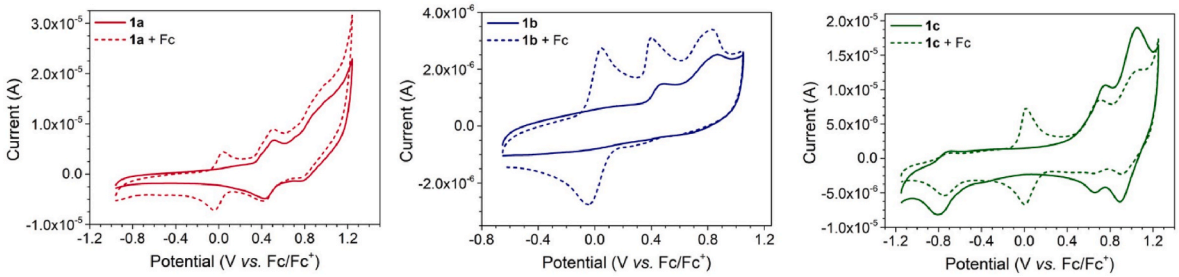

Fig. 5. Cyclic voltammetry plots of dyes **1a-c** in DCM solution, both without and with ferrocene as an internal standard.

E_{ox} values of the dyes thus followed the order of relative strength of their donor groups, with **1c** > **1a** > **1b**. Accordingly, the electrochemical analysis showed that in the case of dye **1b** the E_{ox} value measured in solution was very close to the reported onset of catalysis of a typical Ru^{II}(bda)-based complex (E_{onset}, approx. +1.1 V *vs.* NHE) [81,82], suggesting that a relatively small thermodynamic driving force for hole transfer to the catalyst could exist for such dye. The excited state oxidation potentials (E^*_{ox}) of the dyes were then assessed by subtracting the previously determined $E_{0\text{-}0}$ values from the E_{ox} resulting from cyclic voltammetry, yielding values of −0.98, −1.06 and −0.89 V *vs.* NHE for **1a**, **1b** and **1c**, respectively. These values were more negative than the potential of the conduction band of TiO_2 (estimated at −0.57 V *vs.* NHE at pH = 7), thus suggesting that smooth electron injection into the semiconductor could take place following dye photoexcitation [83]. Therefore, the dyes generally appeared to have appropriate spectroscopic and electrochemical properties to be employed in DS-PEC for water splitting in combination with Ru-based WOCs.

To gather further information on the spectroscopic behavior of the oxidized dyes, a spectroelectrochemical study was finally conducted in DCM solution. The absorption spectra in the UV–vis–NIR region (between 200 and 1600 nm) were recorded under potentiostatic conditions at three different potentials, *i.e.*, one below the first oxidation potential (E_{ox}), representative of the absorption of the neutral species, a second between the first and the second oxidation (E_{ox2}), relevant to the monocationic species, and a third at a potential higher than the second oxidation (di-cation). The results are reported in Fig. 6 while the differential spectra are reported in Fig. S6.

The absorption spectra observed at the potential below E_{ox} (blue curves) are almost coincident with those recorded at open circuit for all dyes **1a-c**. The spectra of the cationic species of dyes **1a** and **1b** at E_{ox} < E < E_{ox2} (green curves) and E > E_{ox2} (red curves) display similar features: (i) the two main absorption bands in the visible region are clearly red-shifted, and (ii) a strong new low-energy absorption band arises, peaking at about 1000 nm (see also Table S4). In the case of **1c** the red shift of the absorption band in the visible region for the cationic species can still be observed, but the absorption band in the NIR is of lower intensity compared to **1a** and **1b**.

3.3.1. *Synthesis of Ru(bda)(PyP)$_2$ complex*

After having prepared and characterized dyes **1a-c**, we turned our attention to the synthesis of the required Ru-based catalyst for water oxidation. We selected previously described compound **Ru(bda)(PyP)$_2$** [44], due to the presence on its structure of two phosphonate anchoring groups for stable attachment to TiO_2, and the reported possibility to easily prepare it from commercially available starting materials. Initially, we attempted the synthesis of **Ru(bda)(PyP)$_2$** by adapting the general procedure described in the literature to access this class of compounds (Scheme S1) [44,81,84]. Accordingly, precursor $RuCl_2(DMSO)_4$ (**11**) was reacted with the tetradentate ligand 2,2′-bipyridine-6,6′-dicarboxylic acid (bda) and NEt_3 to obtain the intermediate complex Ru(bda)$(DMSO)_2$ (**12**), which was not isolated but rather treated *in situ* with diethyl pyridin-4-ylmethylphosphonate (**13**, Scheme S1) to provide di-phosphonic ester complex **14** in good yield (Scheme S1). Unfortunately, at this stage multiple attempts to obtain the final product after conversion of the phosphonic ester moieties to the free acids were unsuccessful. Indeed, when using either $(CH_3)_3SiBr$ or $(CH_3)_3SiI$ as the deprotecting reagent, a complex mixture of products was obtained, from which we were not able to isolate **Ru(bda)(PyP)$_2$** in pure form, also due to its limited solubility in typical organic solvents.

For this reason, the procedure was modified to avoid the last deprotection step (Scheme 3). To this end, complex Ru(bda)$(DMSO)_2$ (**12**) was once again prepared from $RuCl_2(DMSO)_4$ (**11**) under similar conditions as the previous synthesis, but this time the product was isolated by centrifugation and washing with cold methanol. Then, Ru-complex **12** was directly reacted with free pyridin-4-ylmethylphosphonic acid (**15**) dissolved in a 4:1 MeOH/HFIP mixture (HFIP = 1,1,1,3,3,3-hexafluoro-2-propanol). The use of HFIP proved essential to dissolve the otherwise rather insoluble acid **15**, allowing a more efficient formation of the final product, which could then be isolated in good yield by centrifugation and washing with DCM and methanol (Scheme 3). Also in the case of **Ru(bda)(PyP)$_2$**, we found that use of HFIP greatly helped to properly dissolve the compound, facilitating its isolation and further manipulation (*see below*, section 3.6).

3.4. *Spectroscopic characterization on TiO_2 films*

With compounds **1a-c** and **Ru(bda)(PyP)$_2$** in hand, we next

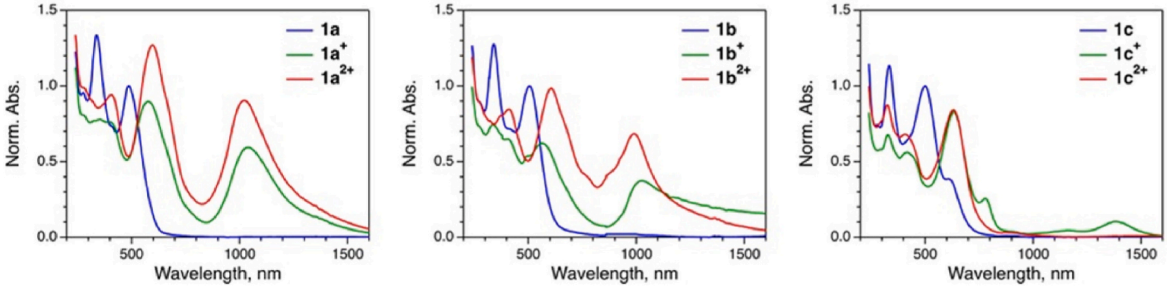

Fig. 6. Absorption spectra of the neutral and cationic species of dyes **1a-c** in $TBAPF_6$ 0.1 M dichloromethane solution.

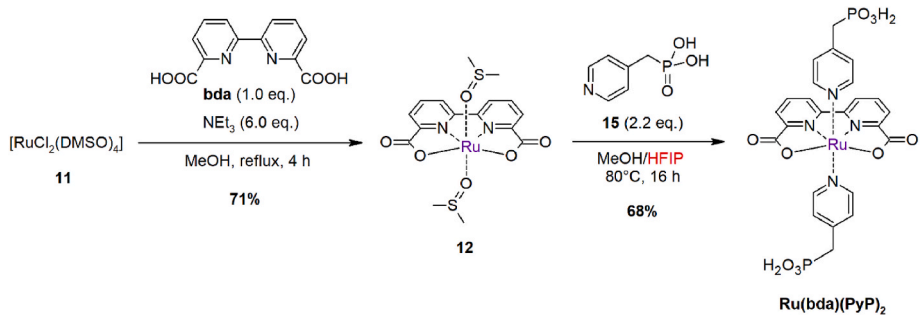

Scheme 3. Synthesis of water oxidation catalyst **Ru(bda)(PyP)$_2$**.

examined their properties after adsorption on mesoporous TiO_2 films deposited on conductive FTO substrates, similar to those later employed for the fabrication of the DS-PEC devices (approx. thickness 5 μm, surface area 1 cm^2, see Materials and Methods Section for details). Dye-sensitized films were obtained by immersing the electrodes for 4 h in 2×10^{-4} M solutions of the dyes in THF, and their UV–Vis absorption spectra are reported in Fig. 7.

Compared to the spectra in solution, only compound **1a** presented a noticeable blue shift of the absorption maximum (482 *vs.* 498 nm), while the other two dyes displayed λ_{max}^{abs} values within 2 nm of those recorded in THF, albeit with a slightly broadened profile and red-shifted onset around 650 nm. The dye loading on TiO_2 (in mol/cm^2) was evaluated from the UV–Vis measurements using Meyer's method [85], by applying the expression $\Gamma = A(\lambda)/[10^3 \cdot \varepsilon(\lambda)]$, where $A(\lambda)$ and $\varepsilon(\lambda)$ represent the absorbance and molar absorptivity at wavelength λ of each dye. The values obtained were 4.1×10^{-8} mol/cm^2 for dye **1a**, 9.3×10^{-8} mol/cm^2 for **1b** and 6.4×10^{-8} mol/cm^2 for **1c**, respectively, which were of the same order of magnitude of those observed for other organic dyes in previous studies [46,51,55]. The spectrum of complex **Ru(bda)(PyP)$_2$** adsorbed on TiO_2 under the same conditions (except for the solvent of the staining solution, which was a 1:9 *v/v* mixture of HFIP/-methanol) resembled that recorded in solution (Fig. S7), with an onset just below 600 nm and a broad but relatively weak absorption encompassing the visible region in the 400–575 nm range (Fig. 7, bottom right). We also measured the absorption spectra of TiO_2 films stained with a solution containing both **1a-c** and **Ru(bda)(PyP)$_2$** in a 2:1 stoichiometric ratio, analogous to that later used for the DS-PEC photoanode preparation (*see below*). In general, the spectra presented similar profiles to those of the dyes alone (Fig. 8), although in the case of **1a** a red-shift of the maximum to 489 nm could be observed, perhaps due to reduction of dye aggregation on TiO_2 surface as a consequence of co-adsorption. Unfortunately, we found it impossible to disentangle the absorption features of the dyes from those of the ruthenium catalyst in the recorded spectra, preventing an estimation of their relative loading on the semiconductor surface with the method described above.

At this stage, to gain a better understanding of the individual processes taking place after light absorption, the dynamics of photoexcitation and charge transfer of the dyes adsorbed on mesoporous TiO_2 films were also studied by means of femtosecond TAS. The temporal evolution of the transient absorption spectra of the three samples is reported in Fig. 9 (left): the spectral characteristics are similar for the three dyes, with a broad band in the 600–800 nm region, an intense band at ca. 900 nm and a broad absorption in the NIR between 1200 nm and 1600 nm.

The decay of the signal follows a complex multi-exponential law all over the vis-NIR spectral range (Fig. S8). Interestingly, the formation of a band at ca. 830 nm is clearly observable (Fig. 9, left, and Fig. S8): it appears with a kinetics in the order of few hundreds of ps, after a fast decay of the signal in the same region, and decays on longer time scales.

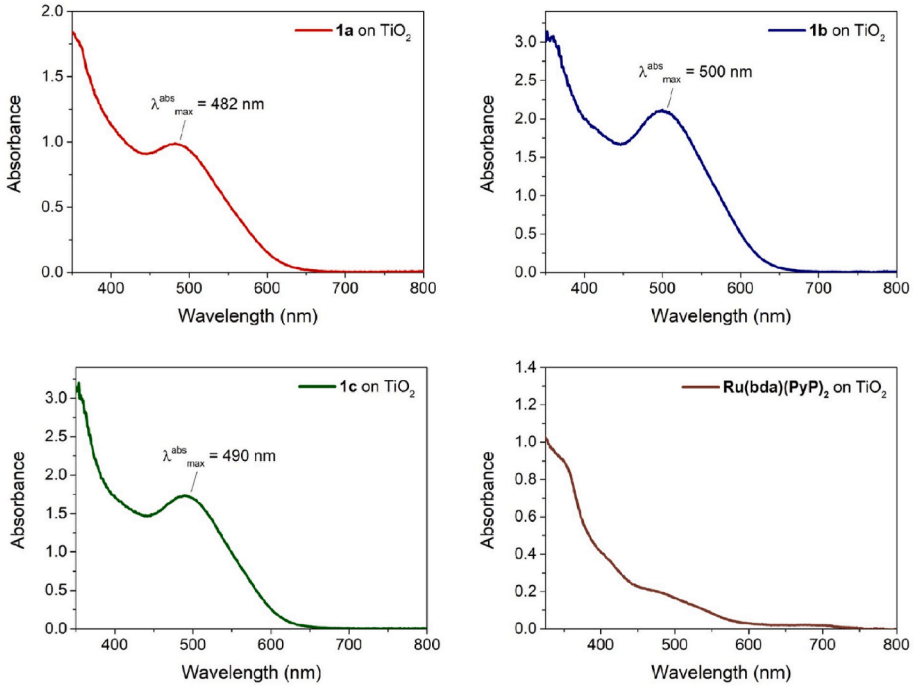

Fig. 7. UV–Vis absorption spectra of dyes **1a-c** and catalyst **Ru(bda)(PyP)$_2$** adsorbed on mesoporous TiO_2 films.

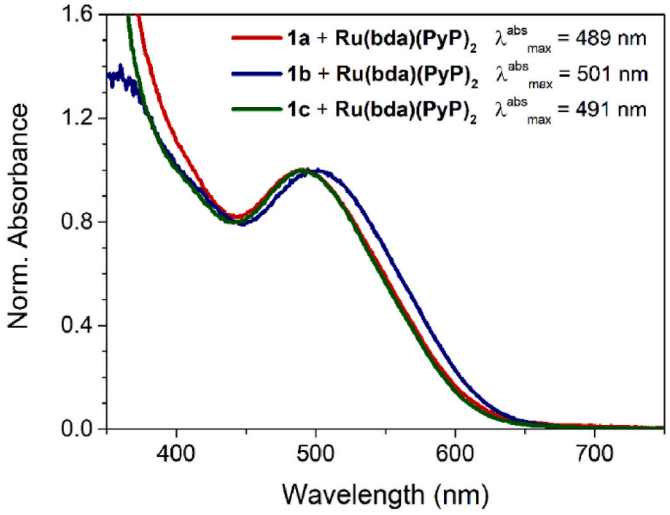

Fig. 8. Normalized UV–Vis absorption spectra of dyes **1a-c** and complex **Ru(bda)(PyP)$_2$** co-adsorbed on TiO_2.

In order to rationalize the data, a global fit analysis has been performed on the transient matrices, and the obtained spectral amplitudes are reported in Fig. 9 (right). In all cases, a fast component of 1–2 ps is associated to a spectral distribution presenting a broad band in the 600–800 nm region and an intense band peaking at ca. 920 nm. Other two main components are identified by the analysis, which markedly differ from the previous one by both spectral features and kinetics. Their spectra are very similar, characterized by a broad band at 600–800 nm, a peak at ca. 830 nm and a broad absorption in the 1200–1600 nm region, and their time constants are in the order of 100–200 ps and >5 ns (infinite lifetime with respect to the time window of the experiment).

We assign the first fast component to the radical cation of the molecule generated upon electron injection into TiO_2, since the spectrum of this species resembles that of the oxidized form of the dye observed by means of spectroelectrochemical analysis (see Fig. 6). The injection of electrons into TiO_2 from the dye singlet excited state is thus an ultrafast process that occurs within the time resolution of the instrument (300 fs). Similar ultrafast injection processes have been reported for titania-supported DSSCs [86,87]. Conversely, the spectral distribution of the components with longer lifetimes can be attributed to the contribution of the dye cation and of both trapped and conduction electrons that forms upon injection, since the latter are reported to absorb at ca. 800 nm and above 1200 nm, respectively [88]. The growth

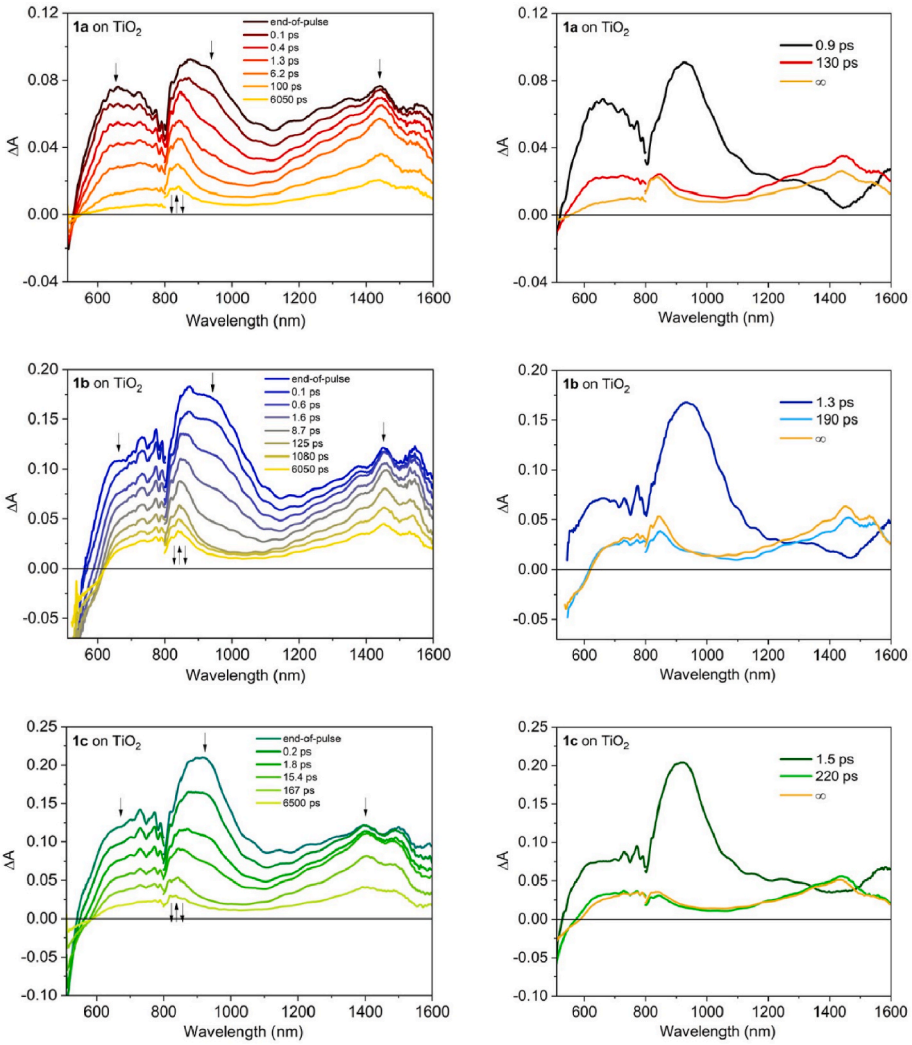

Fig. 9. *Left: transient absorption spectra at different delays of dyes **1a-c** adsorbed on mesoporous TiO_2 films. Right: spectral distribution of pre-exponential amplitudes of calculated lifetimes from global fit analysis.* $\lambda_{exc} = 500$ nm, $E = 3$ μJ/pulse. The spectral region below 510 nm *has been omitted because of the strong noise due to the intense ground state absorption.*

of the band at 830 nm (Fig. S8) testifies the slower accumulation of the trapped electrons with respect to the fast injection event. Interestingly, as mentioned above, these spectra decay with two different time constants: 100–200 ps and >5 ns, as indicated by the global fit (Fig. 9, right). This behaviour can be interpreted considering that charge recombination can occur from two types of electron-hole pairs, one where the electron is still electrostatically bound to the dye cation (interfacial charge-transfer complex) and one where the electron has become a "free" carrier [89]. The "infinite" lifetime is thus indicative of the presence of free electrons that will give origin to the photocurrent. It can be noticed that the short lifetime (1–2 ps) observed for the first component associated with the radical cation of the dye is justified by the absence of an external circuit that promotes the movement of the electron once generated. Part of the formed cations will thus recombine quickly and, given the high attenuation coefficient of these species, their transient features dominate the spectra at short time delays.

When co-adsorbed with the complex **Ru(bda)(PyP)$_2$** on TiO_2, dyes **1a-c** show transient spectral features very similar to those observed for the bare dyes (Figs. S9–S11). Global analysis again reveals three main components with spectral distributions similar to the previous case. A somewhat shorter lifetime is detected for the second component, here in the order of 100–130 ps, indicating a slightly faster charge recombination in interfacial electron-hole couples. Overall, the presence of the Ru complex does not affect the charge injection and charge recombination processes observable in the time scale of the TAS experiment, since the process of regeneration of the dye operated by the catalyst occurs on longer time domains. Besides, the transient absorption features of the bare complex adsorbed on TiO_2 are weak (Fig. S12) and thus hardly recognizable in the spectra of the co-adsorbed samples.

3.5. Electrochemical and photoelectrochemical experiments

As a final part of our study, the capability of the new dyes to work as sensitizers for DS-PEC photoanodes was preliminarily assessed by measuring the relative photocurrent response in a photo-electrochemical cell with three-electrodes configuration and Na_2SO_4 0.1 M water electrolyte. We point out that the aim of these studies was especially to determine if the electrodes were photoactive, measure the extent of photocurrent produced at a fixed potential and compare the relative performances of the dyes under the same conditions, leaving the optimization of cell performances and the precise determination of their efficiency to a future investigation.

Functionalized FTO/nc-TiO_2 electrodes with a surface area of 1 cm^2 (see Materials and Methods Section for details on their preparation) were obtained by simple immersion in the appropriate staining solutions. Electrodes decorated only with the **Ru(bda)(PyP)$_2$** catalyst were prepared by dipping in a 1.0×10^{-4} M solution of the complex in a MeOH/HFIP 9:1 mixture for 4 h. DS-PEC photoanodes, on the other hand, were obtained by immersion in a mixed solution of one of the dyes **1a-c** and **Ru(bda)(PyP)$_2$** in a MeOH/THF/HFIP 70:25:5 solvent mixture for 4 h. The concentrations of the dye and the catalyst in this staining solution were 2.0×10^{-4} M and 1.0×10^{-4} M, respectively. In both cases, the addition of HFIP to the solvent mixture proved essential to obtain a clear solution of the catalyst, allowing its proper adsorption on the semiconductor surface.

Prior to the photoelectrochemical experiments, we recorded the cyclic voltammetry (CV) traces of the electrodes in dark conditions (Figs. S13–S14), using a three-electrodes cell setup with the functionalized films as working electrodes, a Saturated Calomel Electrode (SCE) as the reference electrode, a platinum wire as the counter electrode and phosphate buffer (pH = 6.6) as the electrolyte. In the case of the electrode functionalized with the sole **Ru(bda)(PyP)$_2$**, the small reversible peak at $E_{1/2} \sim +0.6$ V *vs.* NHE could be assigned to the Ru^{II}/Ru^{III} redox couple, whereas an anodic wave with an onset potential of approx. +1.1 V *vs.* NHE (Fig. S13) indicated that the water oxidation reaction occurred [51,81]. As for the DS-PEC photoanodes functionalized with both the dyes and the catalyst, the presence of the Ru complex was confirmed by the same Ru^{II}/Ru^{III} redox peak mentioned above, although the latter was less evident for the sample sensitized with **1b**; the same electrode presented also a smaller water oxidation wave at positive potentials, suggesting that it could be less efficient in promoting the desired reaction (Fig. S14, *see below for a discussion*).

Linear sweep voltammetry (LSV) studies were then carried out in a photo-electrochemical cell, using the functionalized FTO/nc-TiO_2/**1a-c** + **Ru(bda)(PyP)$_2$** films as working electrodes, an Ag/AgCl (KCl sat.) reference electrode and platinum wire as the counter electrode, while aq. Na_2SO_4 0.1 M (pH = 6.5) was employed as the electrolyte. The experiments were conducted under chopped illumination (100 mW cm^{-2}, AM 1.5 calibrated with a reference silicon solar cell), to highlight the different response of the electrode materials and confirm their photoactive behavior (Fig. 10a). The largest photocurrent was provided by dye **1a**, with an onset at around −0.2 V *vs.* NHE and the maximum value of approx. 150 μA cm^{-2} (difference between illuminated and dark conditions) in the +0.4–0.5 V *vs.* NHE range, indicative of its good combination of intense light absorption and well-aligned electrochemical features. Dye **1c** presented a similar behavior, but the value of the photocurrent in this case was smaller, with a maximum of approx. 85 μA cm^{-2} in the same potential range. Conversely, the electrode featuring dye **1b** proved almost inactive under illumination, providing a photocurrent that was just a few μA cm^{-2} higher than that recorded under dark conditions.

In view of the results of the LSV experiments, the subsequent chronoamperometric (CA) experiments were performed at a fixed bias of +0.5 V *vs.* NHE to maximize the photocurrent response (Fig. 10b and c). Current traces were recorded for 100 s, once again under chopped illumination. After an initial decay, caused by fast electron injection from the excited dye to the conduction band of TiO_2 followed by rapid charge recombination (as a result of the kinetic limitations of the dye regeneration process by the WOC) [90], photocurrents remained essentially stable throughout the experiment. The results were in good agreement with those obtained in the LSV experiment, with the **1a**- and **1c**-containing electrodes providing currents of approx. 145 μA cm^{-2} and 82 μA cm^{-2}, respectively, while the electrode fabricated with **1b** showed the by far lowest amount of photocurrent, with a value of just approx. 6 μA cm^{-2}.

The lack of activity shown by the **1b**-containing electrodes could be tentatively explained based on the following reasons: (a) as mentioned above, dye **1b** showed a lower ground state oxidation potential compared to the other two dyes (+1.08 V *vs.* NHE in DCM solution, see Table 2), potentially slowing down its regeneration by the oxidized WOC; (b) in addition, it presented also the highest loading value on TiO_2, suggesting that an insufficient amount of the catalyst could be adsorbed on the semiconductor surface when applying the "co-adsorption" method described above.

Based on these considerations, we reasoned that regeneration of **1b** could be boosted by increasing the relative amount of catalyst adsorbed on the semiconductor relative to the dye. Accordingly, we tested a "sequential" adsorption procedure, in which the bare TiO_2 electrodes were first immersed in a 1.0×10^{-4} M solution of the catalyst for 4 h, and then in a 2.0×10^{-4} M solution of dye **1b**. By comparing the normalized UV–Vis absorption spectra of the electrodes obtained with the two different staining procedures (Fig. S15), a higher relative absorbance was found for the sample obtained with the "sequential" protocol in the 350–500 nm range, where light absorption by the catalyst is larger (see Fig. 6). In addition, in the CV curves (Fig. S16) the redox peak of the Ru^{II}/Ru^{III} couple was more evident for the "sequential" sample and an intense electrocatalytic anodic wave (onset ca. +1.1 V *vs.* NHE) was observed, comparable to that previously obtained with **1a,c**, suggesting that the electrode was more catalytically active than that prepared with the "co-adsorption" procedure.

LSV experiments conducted with the FTO/nc-TiO_2/**1b** + **Ru(bda)(PyP)$_2$** electrodes obtained by the "sequential" adsorption method

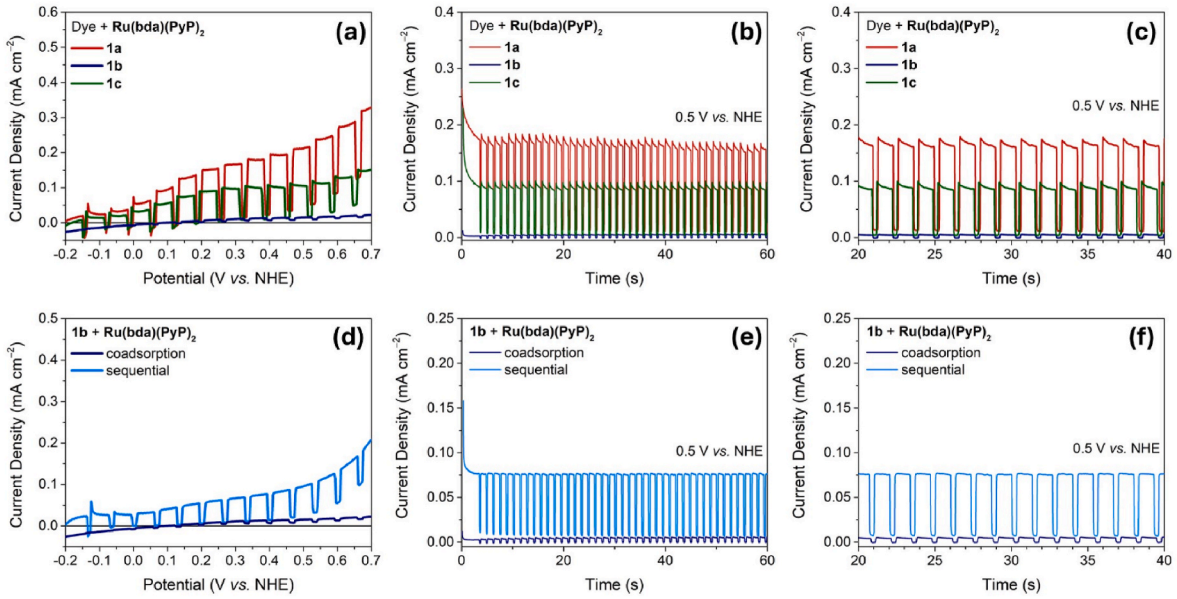

Fig. 10. (a) LSV traces of DS-PEC fabricated with FTO/nc-TiO_2/**dye** + **Ru(bda)(PyP)$_2$** working electrodes under chopped AM 1.5 illumination; (b) CA of the same cells under chopped AM 1.5 illumination from 0 to 60 s; (c) zoom of panel (b) in the 20–40 s range; (d) comparison of the LSV traces of DS-PEC fabricated with FTO/nc-TiO_2/**1b** + **Ru(bda)(PyP)$_2$** working electrodes obtained with the "co-adsorption" and "sequential" methods, under chopped AM 1.5 illumination; (e) CA of the same cells under chopped AM 1.5 illumination from 0 to 60 s; (f) zoom of panel (e) in the 20–40 s range.

indeed displayed an improved photocurrent compared to the previous ones, with a value of approx. 63 μA cm^{-2} in the +0.4–0.5 V *vs.* NHE range (Fig. 10d). This result was once again confirmed by the CA recorded at +0.5 V *vs.* NHE, in which a relatively stable response of approx. 68 μA cm^{-2} could be observed for the entire duration of the experiment. Although the current obtained with the "sequential" **1b** + **Ru(bda)(PyP)$_2$** photoelectrodes was still lower than those provided by dyes **1a,c**, this result was considered highly relevant, as it highlighted how DS-PEC performances could be altered by modifications of the sensitization procedure, in response of the specific structural and electrochemical features of their molecular components.

4. Conclusions

In this paper, we have described our studies concerning the design, synthesis, characterization and application of new donor-acceptor organic dyes as anodic sensitizers in photoelectrochemical cells for water splitting application. With the help of DFT and TD-DFT computational studies, the structures of the dyes were designed to endow them with a precise set of desirable properties, namely: (a) well-aligned ground state oxidation potentials, to allow their regeneration by typical Ru-based water oxidation catalysts; (b) intense visible light absorption, particularly between 500 and 600 nm, as a result of ICT processes; (c) good solubility and anchoring to the electrode semiconductor film.

The structures of dyes **1a-c** presented a common 2,3-diphenyl-5,8-dithienylquinoxaline central core and three different alkoxy-substituted benzene rings as donor groups of moderate strength. The varying number of substituents and the different substitution patterns of the donor groups were expected to alter the energy of the corresponding HOMO levels, allowing a fine tuning of the dyes ground state oxidation potentials and affecting the efficiency of their regeneration by the WOC.

The dyes were prepared through a multistep synthetic sequence, featuring two consecutive direct arylation reactions as the key carbon-carbon bond forming steps. By applying such procedures, it was possible to sequentially introduce both the acceptor and the donor groups while reducing the number of steps compared to typical cross-coupling procedures, keeping the overall synthetic route concise. The spectroscopic and electrochemical properties of compounds **1a-c** were determined both in solution and upon adsorption on mesoporous TiO_2 thin films. In agreement with the results of the computational studies, all compounds presented marked visible light absorption in solution. After adsorption on the semiconductor, spectral profiles were only slightly affected, although a small blue shift of the absorption maxima and a broadening of the main visible absorption bands could be observed. Electrochemical analysis in DCM solution confirmed the expected impact of the relative strength of different donor groups on the ground state oxidation potentials of the compounds, with E_{ox} values increasing in the order **1b** < **1a** < **1c**.

As a WOC to work in combination with the dyes, we selected compound **Ru(bda)(PyP)$_2$**, thanks to its simple symmetric structure and the possibility to prepare it from readily available, commercial starting materials. Its synthetic protocol was slightly modified compared to literature reports, and it was found that using HFIP as a co-solvent was crucial both to improve the efficiency of its formation and facilitate its subsequent purification and handling. CV experiments indicated that the onset of electrochemical water oxidation with **Ru(bda)(PyP)$_2$** adsorbed on TiO_2 occurred at around +1.1 V *vs.* NHE, which was considered compatible with the ground state oxidation potentials of all dyes, although in the case of compound **1b** its lower E_{ox} value measured in solution could point to a less efficient dye-regeneration process in comparison to sensitizers **1a,c**.

Before carrying out the photoelectrochemical tests, the dynamics of photoexcitation and charge transfer of the dyes adsorbed on mesoporous TiO_2 films were studied by means of TAS technique. The results evidenced ultrafast electron injection processes taking place within the time resolution of the instrument, with formation of both dye-bound (lifetime 100–200 ps) and long-lived (>5 ns), "free" charge carriers for all the tested systems, the latter being able to give rise to photocurrent in PEC cells.

Finally, the ability of the new dyes to work as anodic sensitizers in DS-PEC devices was preliminarily assessed by means of photoelectrochemical tests in a three-electrodes cell setup. We found that when the dyes and WOC were deposed on the electrode semiconductor by means of a "co-adsorption" procedure, the best performance was yielded by dye **1a**, which provided a photocurrent density of approx.

150 μA cm^{-2} at +0.5 V *vs.* NHE external bias, while **1c** gave a lower current of approx. 85 μA cm^{-2} at the same bias. The electrodes built with dye **1b**, on the other hand, appeared almost inactive. This was tentatively attributed to the inefficient regeneration of the dye by the WOC, caused both by a lower driving force, as mentioned above, and an insufficient amount of catalyst deposed on the electrode with the "co-adsorption" method. To address this issue, we tested a different staining procedure, involving the sequential deposition on TiO_2 of the WOC followed by the dye. Indeed, under these conditions, a significant photocurrent improvement was observed, although the measured value was still lower than those previously obtained with dyes **1a,c**.

We are confident that the results presented here can contribute to define more general guidelines for the design of organic sensitizers with application in DS-PEC for water splitting. This concerns especially the influence exerted by different donor groups on the electrochemical properties of the compounds and the impact of the central hetero-aromatic moiety on their light harvesting features. In particular, it was confirmed that compounds having a quinoxaline core flanked by highly conjugated thiophene-benzene sections present an intense absorption in the visible region above 500 nm [64], marking a difference from some of the simpler organic dyes previously used in DS-PEC research. Among the new compounds, dye **1a** seemed to possess the most balanced combination of the relevant photophysical and electrochemical properties, presenting intense and broad light absorption, well-aligned ground- and excited state oxidation potentials and optimal adsorption density on TiO_2, resulting in the best photocurrent values of the series. Notably, we also observed that, in the case of the **1b**/**Ru(bda)(PyP)$_2$** combination, changes in the electrode staining procedure, adopted to better accommodate the properties of the molecular components, can have a significant effect on the cells photocurrent response. On the basis of these results, further studies concerning the refinement of the electrode fabrication and functionalization protocols, the exploration of different dye/catalyst combinations and the precise measurement of DS-PEC efficiencies are currently underway.

CRediT authorship contribution statement

Xheila Yzeiri: Writing – review & editing, Methodology, Investigation. **Nicola Sangiorgi:** Writing – review & editing, Methodology, Investigation, Conceptualization. **Francesca Gambassi:** Writing – review & editing, Investigation, Data curation. **Andrea Barbieri:** Writing – review & editing, Investigation, Formal analysis, Data curation. **Massimo Calamante:** Writing – review & editing, Supervision, Methodology, Investigation. **Daniele Franchi:** Writing – review & editing, Methodology, Investigation, Data curation. **Carmen Coppola:** Writing – review & editing, Software, Methodology, Investigation, Formal analysis. **Adalgisa Sinicropi:** Writing – review & editing, Software, Methodology, Investigation, Formal analysis. **Barbara Ventura:** Writing – review & editing, Methodology, Investigation, Formal analysis, Data curation. **Alessandro Mordini:** Writing – review & editing, Validation, Supervision, Funding acquisition, Conceptualization. **Alessandra Sanson:** Writing – review & editing, Supervision, Project administration, Funding acquisition, Conceptualization. **Lorenzo Zani:** Writing – review & editing, Writing – original draft, Supervision, Methodology, Conceptualization.

Declaration of competing interest

The authors declare that they have no known competing financial interests or personal relationships that could have appeared to influence the work reported in this paper.

Data availability

Data will be made available on request.

5. Acknowledgments

The authors thank the National Research Council (Project "RIPRESA - Integrated piezo-phototronic devices for CO_2 reduction to solar liquid fuels", "@CNR" Call), the European Union–Next Generation EU and the Italian Ministry of Environment and Energy Security (POR H_2 AdP MMES/ENEA-CNR-RSE, PNRR–Mission 2, Component 2, Investment 3.5 "Ricerca e sviluppo sull'idrogeno", CUP: B93C22000630006) for financial support.

Appendix A. Supplementary data

Supplementary data to this article can be found online at https://doi.org/10.1016/j.dyepig.2024.112455.

References

[1] Armaroli N, Balzani V. Solar electricity and solar fuels: status and perspectives in the context of the energy transition. Chem Eur J 2016;22:32–57. https://doi.org/10.1002/chem.201503580.
[2] Younas M, Shafique S, Hafeez A, Javed F, Rehman F. An overview of hydrogen production: current status, potential, and challenges. Fuel 2022;316:123317. https://doi.org/10.1016/j.fuel.2022.123317.
[3] Shiva Kumar S, Lim H. An overview of water electrolysis technologies for green hydrogen production. Energy Rep 2022;8:13793–813. https://doi.org/10.1016/j.egyr.2022.10.127.
[4] Burton NA, Padilla RV, Rose A, Habibullah H. Increasing the efficiency of hydrogen production from solar powered water electrolysis. Renew Sustain Energy Rev 2021;135:110255. https://doi.org/10.1016/j.rser.2020.110255.
[5] Jia J, Seitz LC, Benck JD, Huo Y, Chen Y, Ng JWD, Bilir T, Harris JS, Jaramillo TF. Solar water splitting by photovoltaic-electrolysis with a solar-to-hydrogen efficiency over 30%. Nat Commun 2016;7:13237. https://doi.org/10.1038/ncomms13237.
[6] Xu F, Weng B. Photocatalytic hydrogen production: an overview of new advances in structural tuning strategies. J Mater Chem A Mater 2023;11:4473–86. https://doi.org/10.1039/D2TA09614E.
[7] Sohail M, Rauf S, Irfan M, Hayat A, Alghamdi MM, El-Zahhar AA, Ghernaout D, Al-Hadeethi Y, Lv W. Recent developments, advances and strategies in heterogeneous photocatalysts for water splitting. Nanoscale Adv 2024;6:1286–330. https://doi.org/10.1039/D3NA00442B.
[8] Nishiyama H, Yamada T, Nakabayashi M, Maehara Y, Yamaguchi M, Kuromiya Y, Nagatsuma Y, Tokudome H, Akiyama S, Watanabe T, Narushima R, Okunaka S, Shibata N, Takata T, Hisatomi T, Domen K. Photocatalytic solar hydrogen production from water on a 100-m^2 scale. Nature 2021;598:304–7. https://doi.org/10.1038/s41586-021-03907-3.
[9] Hamdani IR, Bhaskarwar AN. Recent progress in material selection and device designs for photoelectrochemical water-splitting. Renew Sustain Energy Rev 2021;138:110503. https://doi.org/10.1016/j.rser.2020.110503.
[10] Liu B, Wang S, Zhang G, Gong Z, Wu B, Wang T, Gong J. Tandem cells for unbiased photoelectrochemical water splitting. Chem Soc Rev 2023;52:4644–71. https://doi.org/10.1039/D3CS00145H.
[11] Yu Z, Li F, Sun L. Recent advances in dye-sensitized photoelectrochemical cells for solar hydrogen production based on molecular components. Energy Environ Sci 2015;8:760–75. https://doi.org/10.1039/c4ee03565h.
[12] Ding X, Zhang L, Wang Y, Liu A, Gao Y. Design of photoanode-based dye-sensitized photoelectrochemical cells assembling with transition metal complexes for visible light-induced water splitting. Coord Chem Rev 2018;357:130–43. https://doi.org/10.1016/j.ccr.2017.10.020.
[13] Zhang S, Ye H, Hua J, Tian H. Recent advances in dye-sensitized photoelectrochemical cells for water splitting. EnergyChem 2019;1:100015. https://doi.org/10.1016/j.enchem.2019.100015.
[14] Sherman BD, McMillan NK, Willinger D, Leem G. Sustainable hydrogen production from water using tandem dye-sensitized photoelectrochemical cells. Nano Converg 2021;8. https://doi.org/10.1186/s40580-021-00257-8.
[15] Muñoz-García AB, Benesperi I, Boschloo G, Concepcion JJ, Delcamp JH, Gibson EA, Meyer GJ, Pavone M, Pettersson H, Hagfeldt A, Freitag M. Dye-sensitized solar cells strike back. Chem Soc Rev 2021;50:12450–550. https://doi.org/10.1039/d0cs01336f.
[16] Li F, Yang H, Li W, Sun L. Device fabrication for water oxidation, hydrogen generation, and CO_2 reduction via molecular engineering. Joule 2018;2:36–60. https://doi.org/10.1016/j.joule.2017.10.012.
[17] Collomb MN, Morales DV, Astudillo CN, Dautreppe B, Fortage J. Hybrid photoanodes for water oxidation combining a molecular photosensitizer with a metal oxide oxygen-evolving catalyst. Sustain Energy Fuels 2019;4:31–49. https://doi.org/10.1039/c9se00597h.
[18] Brennaman MK, Dillon RJ, Alibabaei L, Gish MK, Dares CJ, Ashford DL, House RL, Meyer GJ, Papanikolas JM, Meyer TJ. Finding the way to solar fuels with dye-sensitized photoelectrosynthesis cells. J Am Chem Soc 2016;138:13085–102. https://doi.org/10.1021/jacs.6b06466.

[19] Zhang B, Sun L. Artificial photosynthesis: opportunities and challenges of molecular catalysts. Chem Soc Rev 2019;48:2216–64. https://doi.org/10.1039/c8cs00897c.

[20] Duan L, Bozoglian F, Mandal S, Stewart B, Privalov T, Llobet A, Sun L. A molecular ruthenium catalyst with water-oxidation activity comparable to that of photosystem II. Nat Chem 2012;4:418–23. https://doi.org/10.1038/nchem.1301.

[21] Zhang B, Sun L. Ru-Bda: unique molecular water-oxidation catalysts with distortion induced open site and negatively charged ligands. J Am Chem Soc 2019; 141:5565–80. https://doi.org/10.1021/jacs.8b12862.

[22] Youngblood WJ, Lee SA, Kobayashi Y, Hernandez-Pagan EA, Hoertz PG, Moore TA, Moore AL, Gust D, Mallouk TE. Photoassisted overall water splitting in a visible light-absorbing dye-sensitized photoelectrochemical cell. J Am Chem Soc 2009; 131:926–7. https://doi.org/10.1021/ja809108y.

[23] Youngblood WJ, Lee SHA, Maeda K, Mallouk TE. Visible light water splitting using dye-sensitized oxide semiconductors. Acc Chem Res 2009;42:1966–73. https://doi.org/10.1021/ar9002398.

[24] Brimblecombe R, Koo A, Dismukes GC, Swiegers GF, Spiccia L. Solar driven water oxidation by a bioinspired manganese molecular catalyst. J Am Chem Soc 2010; 132:2892–4. https://doi.org/10.1021/ja910055a.

[25] Zhao Y, Swierk JR, Megiatto JD, Sherman B, Youngblood WJ, Qin D, Lentz DM, Moore AL, Moore TA, Gust D, Mallouk TE. Improving the efficiency of water splitting in dye-sensitized solar cells by using a biomimetic electron transfer mediator. Proc Natl Acad Sci U S A 2012;109:15612–6. https://doi.org/10.1073/pnas.1118339109.

[26] Alibabaei L, Brennaman MK, Norris MR, Kalanyan B, Song W, Losego MD, Concepcion JJ, Binstead RA, Parsons GN, Meyer TJ. Solar water splitting in a molecular photoelectrochemical cell. Proc Natl Acad Sci USA 2013;110:20008–13. https://doi.org/10.1073/pnas.1319628110.

[27] Gao Y, Ding X, Liu J, Wang L, Lu Z, Li L, Sun L. Visible light driven water splitting in a molecular device with unprecedentedly high photocurrent density. J Am Chem Soc 2013;135:4219–22. https://doi.org/10.1021/ja400402d.

[28] Zhang L, Yang X, Wang W, Gurzadyan GG, Li J, Li X, An J, Yu Z, Wang H, Cai B, Hagfeldt A, Sun L. 13.6% Efficient organic dye-sensitized solar cells by minimizing energy losses of the excited state. ACS Energy Lett 2019;4:943–51. https://doi.org/10.1021/acsenergylett.9b00141.

[29] Ji J-M, Zhou H, Eom YK, Kim CH, Kim HK. 14.2% efficiency dye-sensitized solar cells by Co-sensitizing novel thieno[3,2-b]indole-based organic dyes with a promising porphyrin sensitizer. Adv Energy Mater 2020;10:2000124. https://doi.org/10.1002/aenm.202000124.

[30] Ren Y, Zhang D, Suo J, Cao Y, Eickemeyer FT, Vlachopoulos N, Zakeeruddin SM, Hagfeldt A, Grätzel M. Hydroxamic acid pre-adsorption raises the efficiency of cosensitized solar cells. Nature 2023;613:60–5. https://doi.org/10.1038/s41586-022-05460-z.

[31] Decavoli C, Boldrini CL, Manfredi N, Abbotto A. Molecular organic sensitizers for photoelectrochemical water splitting. Eur J Inorg Chem 2020;2020:978–99. https://doi.org/10.1002/ejic.202000026.

[32] Alibabaei L, Sherman BD, Norris MR, Brennaman MK, Meyer TJ. Visible photoelectrochemical water splitting into H_2 and O_2 in a dye-sensitized photoelectrosynthesis cell. Proc Natl Acad Sci USA 2015;112:5899–902. https://doi.org/10.1073/pnas.1506111112.

[33] Lapides AM, Sherman BD, Brennaman MK, Dares CJ, Skinner KR, Templeton JL, Meyer TJ. Synthesis, characterization, and water oxidation by a molecular chromophore-catalyst assembly prepared by atomic layer deposition. The "mummy" strategy. Chem Sci 2015;6:6398–406. https://doi.org/10.1039/c5sc01752a.

[34] Alibabaei L, Dillon RJ, Reilly CE, Brennaman MK, Wee KR, Marquard SL, Papanikolas JM, Meyer TJ. Chromophore-catalyst assembly for water oxidation prepared by atomic layer deposition. ACS Appl Mater Interfaces 2017;9:39018–26. https://doi.org/10.1021/acsami.7b11905.

[35] Liu Q, Wang D, Shan B, Sherman BD, Marquard SL, Eberhart MS, Liu M, Li C, Meyer TJ. Light-driven water oxidation by a dye-sensitized photoanode with a chromophore/catalyst assembly on a mesoporous double-shell electrode. J Chem Phys 2019;150:041727. https://doi.org/10.1063/1.5048780.

[36] Wang D, Niu F, Mortelliti MJ, Sheridan MV, Sherman BD, Zhu Y, McBride JR, Dempsey JL, Shen S, Dares CJ, Li F, Meyer TJ. A stable dye-sensitized photoelectrosynthesis cell mediated by a NiO overlayer for water oxidation. Proc Natl Acad Sci U S A 2020;117:12564–71. https://doi.org/10.1073/pnas.1821687116.

[37] Ding X, Gao Y, Zhang L, Yu Z, Liu J, Sun L. Visible light-driven water splitting in photoelectrochemical cells with supramolecular catalysts on photoanodes. ACS Catal 2014;4:2347–50. https://doi.org/10.1021/cs500518k.

[38] Wang D, Sampaio RN, Troian-Gautier L, Marquard SL, Farnum BH, Sherman BD, Sheridan MV, Dares CJ, Meyer GJ, Meyer TJ. Molecular photoelectrode for water oxidation inspired by photosystem II. J Am Chem Soc 2019;141:7926–33. https://doi.org/10.1021/jacs.9b02548.

[39] Wang D, Xu Z, Sheridan MV, Concepcion JJ, Li F, Lian T, Meyer TJ. Photodriven water oxidation initiated by a surface bound chromophore-donor-catalyst assembly. Chem Sci 2021;12:14441–50. https://doi.org/10.1039/d1sc03896f.

[40] Wang D, Farnum BH, Dares CJ, Meyer TJ. Chemical approaches to artificial photosynthesis: a molecular, dye-sensitized photoanode for O_2 production prepared by layer-by-layer self-assembly. J Chem Phys 2020;152:244706. https://doi.org/10.1063/5.0007383.

[41] Eberhart MS, Wang D, Sampaio RN, Marquard SL, Shan B, Brennaman MK, Meyer GJ, Dares C, Meyer TJ. Water photo-oxidation initiated by surface-bound organic chromophores. J Am Chem Soc 2017;139:16248–55. https://doi.org/10.1021/jacs.7b08317.

[42] Wang D, Eberhart MS, Sheridan MV, Hu K, Sherman BD, Nayak A, Wang Y, Marquard SL, Dares CJ, Meyer TJ. Stabilized photoanodes for water oxidation by integration of organic dyes, water oxidation catalysts, and electron-transfer mediators. Proc Natl Acad Sci U S A 2018;115:8523–8. https://doi.org/10.1073/pnas.1802903115.

[43] Zhu Y, Wang D, Ni W, Gurzadyan GG, Sun L, Meyer TJ, Li F. Water oxidation by a noble metal-free photoanode modified with an organic dye and a molecular cobalt catalyst. J Mater Chem A Mater 2022;10:9121–8. https://doi.org/10.1039/D2TA00573E.

[44] Wee KR, Sherman BD, Brennaman MK, Sheridan MV, Nayak A, Alibabaei L, Meyer TJ. An aqueous, organic dye derivatized SnO_2/TiO_2 core/shell photoanode. J Mater Chem A Mater 2016;4:2969–75. https://doi.org/10.1039/c5ta06678f.

[45] Luo T, Li XA, Bai CJ, Lv CY, Huang JF, Liu JM. Bias-free photoelectrochemical water splitting cells constructed by calixarene dyes and molecular Ru catalysts via pyridyl anchoring groups. ACS Appl Energy Mater 2021;4:14671–80. https://doi.org/10.1021/acsaem.1c03301.

[46] Eom YK, Nhon L, Leem G, Sherman BD, Wang D, Troian-Gautier L, Kim S, Kim J, Meyer TJ, Reynolds JR, Schanze KS. Visible-light-driven photocatalytic water oxidation by a π-conjugated donor-acceptor-donor chromophore/catalyst assembly. ACS Energy Lett 2018;3:2114–9. https://doi.org/10.1021/acsenergylett.8b01020.

[47] Nhon L, Shan B, Taggart AD, Wolfe RMW, Li TT, Klug CM, Nayak A, Bullock RM, Cahoon JF, Meyer TJ, Schanze KS, Reynolds JR. Influence of surface and structural variations in donor-acceptor-donor sensitizers on photoelectrocatalytic water splitting. ACS Appl Mater Interfaces 2021;13:47499–510. https://doi.org/10.1021/acsami.1c11879.

[48] Manfredi N, Boldrini CL, Abbotto A. Organic sensitizers for photoanode water splitting in dye-sensitized photoelectrochemical cells. ChemElectroChem 2018;5: 2395–402. https://doi.org/10.1002/celc.201800592.

[49] Shen L, Zhang S, Ding H, Niu F, Chu Y, Wu W, Hu Y, Hu K, Hua J. Pure organic quinacridone dyes as dual sensitizers in tandem photoelectrochemical cells for unassisted total water splitting. Chem Commun 2021;57:5634–7. https://doi.org/10.1039/d1cc01570b.

[50] Kirner JT, Finke RG. Sensitization of nanocrystalline metal oxides with a phosphonate-functionalized perylene diimide for photoelectrochemical water oxidation with a CoO_x catalyst. ACS Appl Mater Interfaces 2017;9:27625–37. https://doi.org/10.1021/acsami.7b05874.

[51] Yamamoto M, Nishizawa Y, Chábera P, Li F, Pascher T, Sundström V, Sun L, Imahori H. Visible light-driven water oxidation with a subporphyrin sensitizer and a water oxidation catalyst. Chem Commun 2016;52:13702–5. https://doi.org/10.1039/c6cc07877j.

[52] Orbelli Biroli A, Tessore F, Di Carlo G, Pizzotti M, Benazzi E, Gentile F, Berardi S, Bignozzi CA, Argazzi R, Natali M, Sartorel A, Caramori S. Fluorinated Zn^{II} porphyrins for dye-sensitized aqueous photoelectrosynthetic cells. ACS Appl Mater Interfaces 2019;11:32895–908. https://doi.org/10.1021/acsami.9b08042.

[53] Yamamoto M, Wang L, Li F, Fukushima T, Tanaka K, Sun L, Imahori H. Visible light-driven water oxidation using a covalently-linked molecular catalyst–sensitizer dyad assembled on a TiO_2 electrode. Chem Sci 2016;7:1430–9. https://doi.org/10.1039/C5SC03669K.

[54] Antón-García D, Warnan J, Reisner E. A diketopyrrolopyrrole dye-based dyad on a porous TiO_2 photoanode for solar-driven water oxidation. Chem Sci 2020;11: 12769–76. https://doi.org/10.1039/D0SC04509H.

[55] Decavoli C, Boldrini CL, Trifiletti V, Luong S, Fenwick O, Manfredi N, Abbotto A. Dye-catalyst dyads for photoelectrochemical water oxidation based on metal-free sensitizers. RSC Adv 2021;11:5311–9. https://doi.org/10.1039/d0ra10971a.

[56] Decavoli C, Boldrini CL, Faroldi F, Baldini L, Sansone F, Ranaudo A, Greco C, Cosentino U, Moro G, Manfredi N, Abbotto A. Calix[4]arene-Based sensitizers for host-guest supramolecular dyads for solar energy conversion in photoelectrochemical cells. European J Org Chem 2022;2022:e202200649. https://doi.org/10.1002/ejoc.202200649.

[57] Dessì A, Monai M, Bessi M, Montini T, Calamante M, Mordini A, Reginato G, Trono C, Fornasiero P, Zani L. Towards sustainable H_2 production: rational design of hydrophobic triphenylamine-based dyes for sensitized ethanol photoreforming. ChemSusChem 2018;11:793–805. https://doi.org/10.1002/cssc.201701707.

[58] Bettucci O, Skaltsas T, Calamante M, Dessì A, Bartolini M, Sinicropi A, Filippi J, Reginato G, Mordini A, Fornasiero P, Zani L. Combining dithienosilole-based organic dyes with a brookite/platinum photocatalyst toward enhanced visible-light-driven hydrogen production. ACS Appl Energy Mater 2019;2:5600–12. https://doi.org/10.1021/acsaem.9b00782.

[59] Bartolini M, Gombac V, Sinicropi A, Reginato G, Dessì A, Mordini A, Filippi J, Montini T, Calamante M, Fornasiero P, Zani L. Tuning the properties of benzothiadiazole dyes for efficient visible light-driven photocatalytic H_2 production under different conditions. ACS Appl Energy Mater 2020;3:8912–28. https://doi.org/10.1021/acsaem.0c01391.

[60] Salerno G, Cecconi B, Bettucci O, Monai M, Zani L, Franchi D, Calamante M, Mordini A, Montini T, Fornasiero P, Manfredi N, Abbotto A. Enhanced long-term stability of a photosensitizer with a hydroxamic acid anchor in dye-sensitized photocatalytic hydrogen generation. European J Org Chem 2023;26:e202300924. https://doi.org/10.1002/ejoc.202300924.

[61] Zani L, Melchionna M, Montini T, Fornasiero P. Design of dye-sensitized TiO_2 materials for photocatalytic hydrogen production: light and shadow. JPhys Energy 2021;3:031001. https://doi.org/10.1088/2515-7655/abe04b.

[62] Yashwantrao G, Saha S. Perspective on the rational design strategies of quinoxaline derived organic sensitizers for dye-sensitized solar cells (DSSC). Dyes Pigments 2022;199:110093. https://doi.org/10.1016/j.dyepig.2022.110093.

[63] Papucci C, Charaf R, Coppola C, Sinicropi A, Di Donato M, Taddei M, Foggi P, Battisti A, De Jong B, Zani L, Mordini A, Pucci A, Calamante M, Reginato G. Luminescent solar concentrators with outstanding optical properties by employment of D-A-D quinoxaline fluorophores. J Mater Chem C Mater 2021;9:15608–21. https://doi.org/10.1039/d1tc02923a.

[64] Goti G, Reginato G, Coppola C, Dessì A, Franchi D, Mordini A, Picchi A, Pucci A, Sinicropi A, Zani L, Calamante M. Green light-responsive D-π-A-π-D quinoxaline emitters for luminescent solar concentrators: potential integration in agrivoltaic systems. European J Org Chem 2024:e202400112. https://doi.org/10.1002/ejoc.202400112.

[65] Ji J-M, Zhou H, Kim HK. Rational design criteria for D–π–A structured organic and porphyrin sensitizers for highly efficient dye-sensitized solar cells. J Mater Chem A Mater 2018;6:14518–45. https://doi.org/10.1039/C8TA02281J.

[66] Qiao H, Deng Y, Peng R, Wang G, Yuan J, Tan S. Effect of π-spacers and anchoring groups on the photovoltaic performances of ullazine-based dyes. RSC Adv 2016;6:70046–55. https://doi.org/10.1039/C6RA11918B.

[67] Almenningen DM, Haga BS, Hansen HE, Buene AF, Hoff BH, Gautun OR. Adamantyl side chains as anti-aggregating moieties in dyes for dye-sensitized solar cells. Chem Eur J 2022;28:e202201726. https://doi.org/10.1002/chem.202201726.

[68] Liu D, Chen M, Li K, Li Z, Huang J, Wang J, Jiang Z, Zhang Z, Xie T, Newkome GR, Wang P. Giant truncated metallo-tetrahedron with unexpected supramolecular aggregation induced emission enhancement. J Am Chem Soc 2020;142:7987–94. https://doi.org/10.1021/jacs.0c02366.

[69] Pratap Tripathi N, Gupta V, Tarun T, Kumar Pandey U, Sengupta S. Functionalized benzothiadiazole non-fused A−D−A'−D−A small molecules for effective electron mobilities and metal-free photocatalysis. Chem Eur J 2023;29:e202203951. https://doi.org/10.1002/chem.202203951.

[70] Putri SK, Kim YH, Whang DR, Lee MS, Kim JH, Chang DW. Step-by-step improvement in photovoltaic properties of fluorinated quinoxaline-based low-band-gap polymers. Org Electron 2017;47:14–23. https://doi.org/10.1016/j.orgel.2017.04.025.

[71] Aranzaes JR, Daniel M-C, Astruc D. Metallocenes as references for the determination of redox potentials by cyclic voltammetry - permethylated iron and cobalt sandwich complexes, inhibition by polyamine dendrimers, and the role of hydroxy-containing ferrocenes. Can J Chem 2006;84:288–99. https://doi.org/10.1139/v05-262.

[72] Hohenberg P, Kohn W. Inhomogeneous electron gas. Phys Rev 1964;136:B864–71. https://doi.org/10.1103/PhysRev.136.B864.

[73] Kohn W, Sham LJ. Self-consistent equations including exchange and correlation effects. Phys Rev 1965;140:A1133–8. https://doi.org/10.1103/PhysRev.140.A1133.

[74] Adamo C, Jacquemin D. The calculations of excited-state properties with time-dependent density functional theory. Chem Soc Rev 2013;42:845–56. https://doi.org/10.1039/C2CS35394F.

[75] Laurent AD, Adamo C, Jacquemin D. Dye chemistry with time-dependent density functional theory. Phys Chem Chem Phys 2014;16:14334–56. https://doi.org/10.1039/C3CP55336A.

[76] Frisch MJ, Trucks GW, Schlegel HB, Scuseria GE, Robb MA, Cheeseman JR, Scalmani G, Barone V, Petersson GA, Nakatsuji H, Li X, Caricato M, Marenich AV, Bloino J, Janesko BG, Gomperts R, Mennucci B, Hratchian HP, Ortiz JV, Izmaylov AF, Sonnenberg JL, Williams-Young D, Ding F, Lipparini F, Egidi F, Goings J, Peng B, Petrone A, Henderson T, Ranasinghe D, Zakrzewski VG, Gao J, Rega N, Zheng G, Liang W, Hada M, Ehara M, Toyota K, Fukuda R, Hasegawa J, Ishida M, Nakajima T, Honda Y, Kitao O, Nakai H, Vreven T, Throssell K, Montgomery Jr JA, Peralta JE, Ogliaro F, Bearpark MJ, Heyd JJ, Brothers EN, Kudin KN, Staroverov VN, Keith TA, Kobayashi R, Normand J, Raghavachari K, Rendell AP, Burant JC, Iyengar SS, Tomasi J, Cossi M, Millam JM, Klene M, Adamo C, Cammi R, Ochterski JW, Martin RL, Morokuma K, Farkas O, Foresman JB, Fox DJ. Gaussian 16. 2016.

[77] Tomasi J, Mennucci B, Cammi R. Quantum mechanical continuum solvation models. Chem Rev 2005;105:2999–3094. https://doi.org/10.1021/cr9904009.

[78] Yanai T, Tew DP, Handy NC. A new hybrid exchange–correlation functional using the Coulomb-attenuating method (CAM-B3LYP). Chem Phys Lett 2004;393:51–7. https://doi.org/10.1016/j.cplett.2004.06.011.

[79] Lynch BJ, Fast PL, Harris M, Truhlar DG. Adiabatic connection for kinetics. J Phys Chem A 2000;104:4811–5. https://doi.org/10.1021/jp000497z.

[80] Zani L, Dessì A, Franchi D, Calamante M, Reginato G, Mordini A. Transition metal-catalyzed cross-coupling methodologies for the engineering of small molecules with applications in organic electronics and photovoltaics. Coord Chem Rev 2019;392:177–236. https://doi.org/10.1016/J.CCR.2019.04.007.

[81] Gao Y, Zhang L, Ding X, Sun L. Artificial photosynthesis-functional devices for light driven water splitting with photoactive anodes based on molecular catalysts. Phys Chem Chem Phys 2014;16:12008–13. https://doi.org/10.1039/c3cp55204g.

[82] Sheridan MV, Sherman BD, Marquard SL, Fang Z, Ashford DL, Wee K-R, Gold AS, Alibabaei L, Rudd JA, Coggins MK, Meyer TJ. Electron transfer mediator effects in water oxidation catalysis by solution and surface-bound ruthenium bpy-dicarboxylate complexes. J Phys Chem C 2015;119:25420–8. https://doi.org/10.1021/acs.jpcc.5b08326.

[83] Kavan L, Tétreault N, Moehl T, Grätzel M. Electrochemical characterization of TiO_2 blocking layers for dye-sensitized solar cells. J Phys Chem C 2014;118:16408–18. https://doi.org/10.1021/jp4103614.

[84] Staehle R, Tong L, Wang L, Duan L, Fischer A, Ahlquist MSG, Sun L, Rau S. Water oxidation catalyzed by mononuclear ruthenium complexes with a 2,2′-Bipyridine-6,6′-dicarboxylate (bda) ligand: how ligand environment influences the catalytic behavior. Inorg Chem 2014;53:1307–19. https://doi.org/10.1021/ic401701z.

[85] Chen Z, Concepcion JJ, Jurss JW, Meyer TJ. Single-site, catalytic water oxidation on oxide surfaces. J Am Chem Soc 2009;131:15580–1. https://doi.org/10.1021/ja906391w.

[86] Gierszewski M, Glinka A, Grądzka I, Gierczyk B, Ziółek M. Testing new concepts in solar cells sensitized with indoline dyes—alkoxysilyl anchoring group, molecular capping, and cobalt-based electrolyte. J Phys Chem C 2018;122:25764–75. https://doi.org/10.1021/acs.jpcc.8b06389.

[87] Idígoras J, Sobuś J, Jancelewicz M, Azaceta E, Tena-Zaera R, Anta JA, Ziółek M. Effect of different photoanode nanostructures on the initial charge separation and electron injection process in dye sensitized solar cells: a photophysical study with indoline dyes. Mater Chem Phys 2016;170:218–28. https://doi.org/10.1016/j.matchemphys.2015.12.042.

[88] Yoshihara T, Katoh R, Furube A, Tamaki Y, Murai M, Hara K, Murata S, Arakawa H, Tachiya M. Identification of reactive species in photoexcited nanocrystalline TiO_2 films by wide-wavelength-range (400−2500 nm) transient absorption spectroscopy. J Phys Chem B 2004;108:3817–23. https://doi.org/10.1021/jp031305d.

[89] Virkki K, Tervola E, Ince M, Torres T, Tkachenko NV. Comparison of electron injection and recombination on TiO 2 nanoparticles and ZnO nanorods photosensitized by phthalocyanine. R Soc Open Sci 2018;5:180323. https://doi.org/10.1098/rsos.180323.

[90] Kirner JT, Stracke JJ, Gregg BA, Finke RG. Visible-light-assisted photoelectrochemical water oxidation by thin films of a phosphonate-functionalized perylene diimide plus CoOx cocatalyst. ACS Appl Mater Interfaces 2014;6:13367–77. https://doi.org/10.1021/am405598w.